



**HAL**  
open science

## Insights into the Rich Polymorphism of the Na<sup>+</sup> Ion Conductor Na<sub>3</sub>PS<sub>4</sub> from the Perspective of Variable-Temperature Diffraction and Spectroscopy

Theodosios Famprakis, Houssny Bouyanfif, Pieremanuele Canepa, Mohamed Zbiri, James A Dawson, Emmanuelle Suard, François Fauth, Helen y Playford, Damien Dambournet, Olaf J Borkiewicz, et al.

### ► To cite this version:

Theodosios Famprakis, Houssny Bouyanfif, Pieremanuele Canepa, Mohamed Zbiri, James A Dawson, et al.. Insights into the Rich Polymorphism of the Na<sup>+</sup> Ion Conductor Na<sub>3</sub>PS<sub>4</sub> from the Perspective of Variable-Temperature Diffraction and Spectroscopy. *Chemistry of Materials*, 2021, 33 (14), pp.5652 - 5667. 10.1021/acs.chemmater.1c01113 . hal-03355393

**HAL Id: hal-03355393**

<https://hal.sorbonne-universite.fr/hal-03355393v1>

Submitted on 27 Sep 2021

**HAL** is a multi-disciplinary open access archive for the deposit and dissemination of scientific research documents, whether they are published or not. The documents may come from teaching and research institutions in France or abroad, or from public or private research centers.

L'archive ouverte pluridisciplinaire **HAL**, est destinée au dépôt et à la diffusion de documents scientifiques de niveau recherche, publiés ou non, émanant des établissements d'enseignement et de recherche français ou étrangers, des laboratoires publics ou privés.

# Insights into the Rich Polymorphism of the Na<sup>+</sup> Ion Conductor Na<sub>3</sub>PS<sub>4</sub> from the Perspective of Variable-Temperature Diffraction and Spectroscopy

Theodosios Famprikis,\* Houssny Bouyanfif, Pieremanuele Canepa, Mohamed Zbiri, James A. Dawson, Emmanuelle Suard, François Fauth, Helen Y. Playford, Damien Dambournet, Olaf J. Borkiewicz, Matthieu Courty, Oliver Clemens, Jean-Noël Chotard, M. Saiful Islam,\* and Christian Masquelier\*



Cite This: *Chem. Mater.* 2021, 33, 5652–5667



Read Online

ACCESS |



Metrics & More

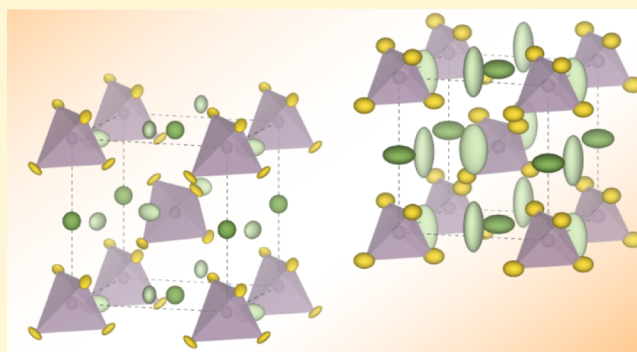


Article Recommendations



Supporting Information

**ABSTRACT:** Solid electrolytes are crucial for next-generation solid-state batteries, and Na<sub>3</sub>PS<sub>4</sub> is one of the most promising Na<sup>+</sup> conductors for such applications, despite outstanding questions regarding its structural polymorphs. In this contribution, we present a detailed investigation of the evolution in structure and dynamics of Na<sub>3</sub>PS<sub>4</sub> over a wide temperature range 30 < T < 600 °C through combined experimental–computational analysis. Although Bragg diffraction experiments indicate a second-order phase transition from the tetragonal ground state (α, P4̄2<sub>1</sub>c) to the cubic polymorph (β, I4̄3m) above ~250 °C, pair distribution function analysis in real space and Raman spectroscopy indicate remnants of a tetragonal character in the range 250 < T < 500 °C, which we attribute to dynamic local tetragonal distortions. The first-order phase transition to the mesophasic high-temperature polymorph (γ, Fddd) is associated with a sharp volume increase and the onset of liquid-like dynamics for sodium-cations (translational) and thiophosphate-polyanions (rotational) evident by inelastic neutron and Raman spectroscopies, as well as pair-distribution function and molecular dynamics analyses. These results shed light on the rich polymorphism of Na<sub>3</sub>PS<sub>4</sub> and are relevant for a range host of high-performance materials deriving from the Na<sub>3</sub>PS<sub>4</sub> structural archetype.



## INTRODUCTION

Battery technology is the key to the electrification of transport and the integration of renewable energy into the grid. The push to improve on the current state-of-the-art lithium-ion battery technology has converged toward the investigation of various post-lithium-ion concepts and among them, solid-state batteries which rely on the substitution of the liquid electrolyte with solid ion conductors.<sup>1,2</sup> In parallel, economic and geopolitical considerations over the availability of lithium have motivated research on sodium analogues of the lithium(-ion) battery chemistries.<sup>3</sup> The above strategies and their advantages can be combined in solid-state sodium(-ion) batteries which rely on fast Na<sup>+</sup> conductors.

Sodium orthothiophosphate (Na<sub>3</sub>PS<sub>4</sub>) is the archetypal member of a very promising family of Na<sup>+</sup> conductors, with a distinct crystal structure compared to the compositionally analogous thio-LISICON (e.g., Li<sub>3</sub>PS<sub>4</sub>).<sup>4</sup> Na<sub>3</sub>PS<sub>4</sub> has attracted considerable attention as a potential solid electrolyte material for sodium-based solid-state batteries due to its facile synthesis<sup>5–7</sup> and its high ionic conductivity, up to the mS/

cm range.<sup>8</sup> Solid-state battery prototypes based on Na<sub>3</sub>PS<sub>4</sub> have already been demonstrated in the laboratory scale.<sup>9–15</sup>

At the same time, the Na<sub>3</sub>PS<sub>4</sub> structural archetype has proven to be a fertile playground for material design through elemental substitutions, defining a wider materials family of the general composition Na<sub>3</sub>PnCh<sub>4</sub> (Pn: pnictogens P, As, Sb; Ch: chalcogens S, Se),<sup>16–30</sup> which is receptive to various aliovalent substitutions, for example, Ca<sup>2+</sup> on the sodium sites,<sup>31</sup> Cl<sup>-</sup> on the chalcogenide site,<sup>4,32–35</sup> and Si<sup>4+</sup> or W<sup>6+</sup> on the pnictide site.<sup>36–44</sup> Notable compositions of the Na<sub>3</sub>PS<sub>4</sub> structural family include Na<sub>3</sub>SbS<sub>4</sub> with a room-temperature conductivity of the order 10<sup>-3</sup> S/cm and distinct stability against ambient moisture<sup>22,25,26</sup> and the recently reported tungsten-doped Na<sub>3-x</sub>W<sub>x</sub>Sb<sub>1-x</sub>S<sub>4</sub> with room-temperature Na<sup>+</sup>-conductivity of

Received: March 31, 2021

Revised: June 4, 2021

Published: July 16, 2021



the order  $10^{-2}$  S/cm,<sup>39,40</sup> currently the highest reported among polycrystalline  $\text{Na}^+$  and  $\text{Li}^+$  conductors.

In recent contributions, we have examined the effect of mechanochemical synthesis and pressure application on the room-temperature structure and dynamics of  $\text{Na}_3\text{PS}_4$ <sup>45</sup> and brought to light a new high-temperature polymorph with plastic crystal characteristics,<sup>46</sup> highlighting the need to fully characterize the multiscale structure of this important Na-ion conductor and its dependence on temperature, pressure, and synthesis conditions. Here, we explore the evolution in the structure and dynamics of well-crystallized  $\text{Na}_3\text{PS}_4$  samples with temperature through diffraction [Bragg and pair distribution function (PDF)], spectroscopy [Raman and inelastic neutron scattering (INS)], and associated theoretical analyses with a focus on the accurate description of the nature of the different polymorphs and phase transitions.

## RESULTS

The sample investigated in this study is a polycrystalline powder of  $\text{Na}_3\text{PS}_4$  synthesized through a solid-state route from a stoichiometric mixture of  $\text{Na}_2\text{S}$  and  $\text{P}_2\text{S}_5$ , as first demonstrated by Jansen and Henseler<sup>47</sup> (see [Methods](#)).

**Diffraction Analysis.** Variable-temperature Bragg diffraction experiments shown in [Figure 1a](#) reveal the evolution of the average structure of  $\text{Na}_3\text{PS}_4$  in the range 35–550 °C. A smooth, continuous evolution of the diffractograms is observed in the range 35–500 °C corresponding to the  $\alpha$ - and  $\beta$ -

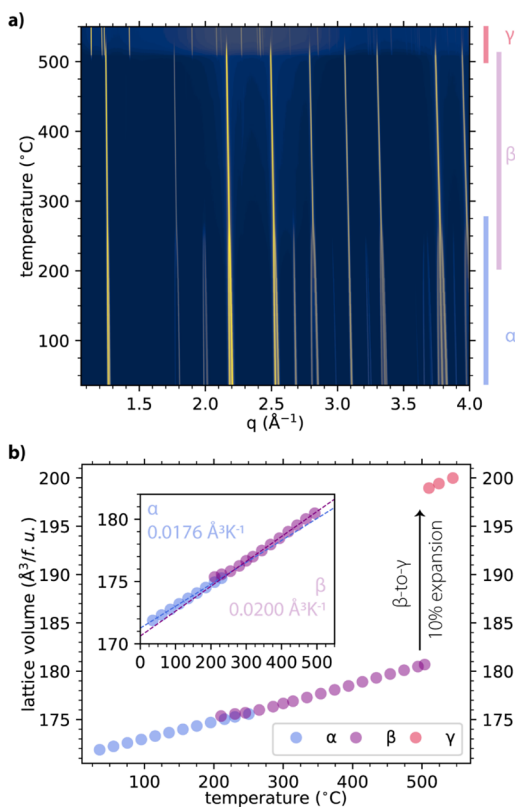


**Figure 1.** Variable-temperature X-ray Bragg diffraction experiments on  $\text{Na}_3\text{PS}_4$  in the range 35–550 °C. (a) Contour plot of the diffractograms as a function of temperature. (b) Evolution of the crystallographic lattice volume as a function of temperature. Inset: Magnification of the previous panel highlighting a slight change in slope between the cubic and the tetragonal polymorphs. Only a subset of available data points is plotted in (b) for clarity.

polymorphs of  $\text{Na}_3\text{PS}_4$ .<sup>47,48</sup> The characteristic peak merging and extinction related to the tetragonal-to-cubic transition is observed in the range 200–300 °C. Above 500 °C,  $\text{Na}_3\text{PS}_4$  transforms into the recently discovered plastic  $\gamma$ -polymorph.<sup>46</sup> Representative fits of the neutron and X-ray Bragg diffractograms for each polymorph are shown in the [Supporting Information](#) (Figures S1–S3, Tables S1–S3).

The lattice volume, extracted from the diffractogram refinements and plotted in [Figure 1b](#), shows a smooth evolution with temperature in the range 35–500 °C with no discontinuity along the  $\alpha$ -to- $\beta$  transition. In this temperature range, the relationship between the lattice volume and temperature remains linear with a slight change of slope corresponding to the  $\alpha$ -to- $\beta$  transition. The thermal expansion coefficient calculated for the  $\alpha$ -phase from the slope of the  $V$  versus  $T$  plot in the range 30–200 °C amounts to  $\sim 1.0 \times 10^{-4}$   $\text{K}^{-1}$  (referenced to the volume at 30 °C). This value increases slightly upon transition to  $\sim 1.1 \times 10^{-4}$   $\text{K}^{-1}$  as calculated for the range 300–500 °C (referenced to the volume at 300 °C). In contrast, the  $\beta$ -to- $\gamma$  transition is associated with a large discontinuity in lattice volume involving a sizeable  $\sim 10\%$  expansion. The phase transitions and volume evolution are fully reversible on cooling, albeit with certain hysteresis on the transition temperatures notably for the  $\gamma$ -to- $\beta$  transition ([Figure S4](#)). In addition, there are some changes in the relative intensities of Bragg peaks of the  $\alpha$ - and  $\beta$ -phases on cooling, which we attribute to the anisotropic growth of these phases in preferential orientations upon recrystallization from the  $\gamma$ -phase.

We further investigated the evolution of the local structure through total diffraction experiments using X-ray and neutrons. From such experiments, we extracted the PDF which represents a “weighted histogram of the interatomic distances” in the material. The evolution of the X-ray PDF in the range 30–600 °C is plotted in [Figure 2](#) and annotated with the pairwise interatomic distances corresponding to the room-temperature structure of  $\alpha$ - $\text{Na}_3\text{PS}_4$ .

Upon heating, most PDF peaks broaden and shift to higher distances continuously, signatures of the increased atomic mobility and of the expansion of the crystalline lattice, respectively. No discontinuous change in the local structure can be observed corresponding to the  $\alpha$ -to- $\beta$  transition at  $\sim 250$  °C. The neutron PDFs of the  $\alpha$  and  $\beta$  polymorphs, measured at 30 and 300 °C, respectively, can be well fit through small-box Rietveld-type refinements in the tetragonal  $P4_21c$  framework ([Figures S5 and S6](#)). On the other hand, most interatomic correlations vanish completely upon the phase transition to the  $\gamma$ -phase, observed here at  $\sim 470$  °C.<sup>e</sup> Both neutron and X-ray measurements corroborate this observation ([Figure S8](#)). Continuous peak broadening is to be expected at higher temperatures from increased thermal motion, but the discontinuous vanishing of most peaks indicates a transition to a liquid-like local structure in the  $\gamma$ -phase. The sole peaks that persist beyond the  $\beta$ -to- $\gamma$  transition are those corresponding to the nearest-neighbor P–S ( $\sim 2.0$  Å), Na–S ( $\sim 2.8$  Å), and S–S ( $\sim 3.5$  Å) atomic pairs. The first-order P–S pair, corresponding to the P–S bond of the  $\text{PS}_4^{3-}$  anion, is the least affected by the transition showing only a slight broadening. Similar observations can be made for the first order S–S pair corresponding to the S–S correlation in the  $\text{PS}_4^{3-}$  moiety, indicating increased vibrational freedom for the  $\text{PS}_4^{3-}$  anions.

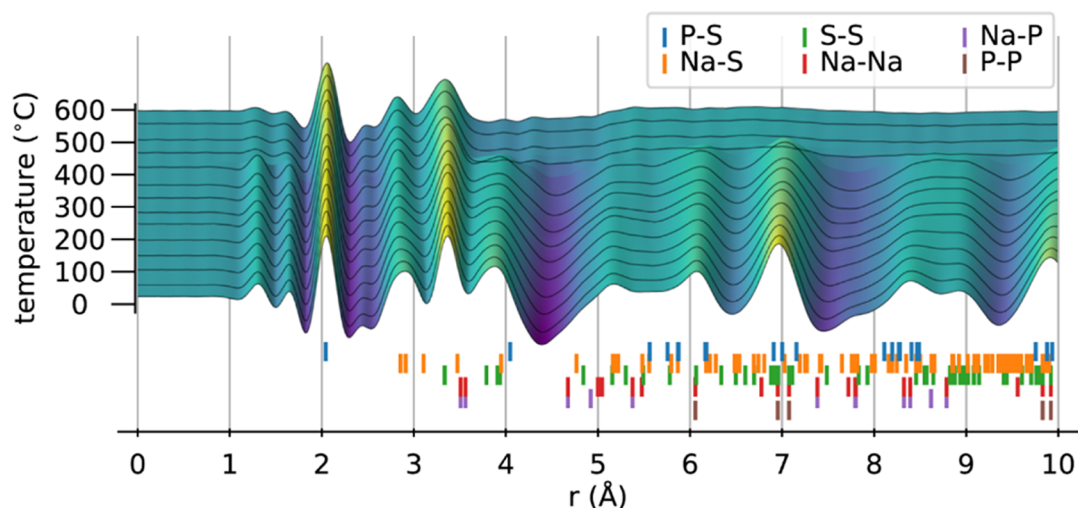


**Figure 2.** Variable-temperature X-ray pair distribution function of  $\text{Na}_3\text{PS}_4$  in the range 0–10 Å as a function of temperature in the range 30–600 °C. Discrete PDFs shown every  $\sim 50$  °C. The distances associated with pairwise correlations at 30 °C are identified for reference. Apparent unindexed peaks at 1.4, 1.7, and 2.4 Å are artifacts of the Fourier transform.

**Vibrational Spectroscopy.** The dynamical properties of  $\text{Na}_3\text{PS}_4$  were investigated by means of variable temperature Raman (Figure 3) and inelastic neutron spectroscopies (Figure 4). To aid in the interpretation of the vibrational spectra, we also performed a group theoretical analysis to derive the vibrational modes at the  $\Gamma$ -point and subsequently performed density functional theory (DFT)-based calculations to simulate the energies and approximate Raman intensities of these said modes. Figure 3a compares the results of calculations with a Raman spectrum collected at 100 K for increased resolution. The agreement between calculated and experimental spectra is excellent. We underline that the calculated frequencies have not been scaled to fit the experimental data. The spectra are dominated by the normal modes of the  $\text{PS}_4^{3-}$  anion, denoted  $\nu_1$ – $\nu_4$ , clearly visible above 210  $\text{cm}^{-1}$ .

The four normal modes of the ideal (isolated)  $\text{PS}_4$  tetrahedron are split into multiple frequencies (degeneracy is lifted), mainly due to the effect of the symmetry reduction in the tetragonal space group:<sup>49,50</sup> in the tetragonal  $\alpha$ -polymorph, the point group symmetry at the phosphorus site ( $S_4$ ) and of the unit cell ( $D_{2d}$ ) are lower than  $T_d$ , leading to three distinct frequencies for each of the asymmetric  $\nu_3$  and  $\nu_4$  modes and to two distinct frequencies of the symmetric bending  $\nu_2$  mode (“static field” or “site group” splitting<sup>49</sup>). Notably, our theoretical analysis indicates that this effect of mode splitting should be absent in the  $\beta$ -polymorph where both the phosphorus site and unit cell point group symmetry are  $T_d$ , as illustrated in Table 1 and elaborated in the Supporting Information.

The frequencies of the Raman modes are accurately predicted from calculation; however, there are certain discrepancies between the calculated and observed intensities in Figure 3a. Most obviously, the intensities of high frequency  $\nu_3$  asymmetric stretching modes at 573 and 575  $\text{cm}^{-1}$  are significantly underestimated in calculations.<sup>b</sup> Lower-energy modes below 210  $\text{cm}^{-1}$  mostly pertain to librations of the  $\text{PS}_4^{3-}$  anions and to translations of the  $\text{Na}^+$  cations (Table 2). Although the intensities of most of these modes are quite low, we can observe a certain few at 100 K and assign them based on the DFT calculations. Most Na displacements take place parallel to the principal axes ([100], [010], and [001]). Given

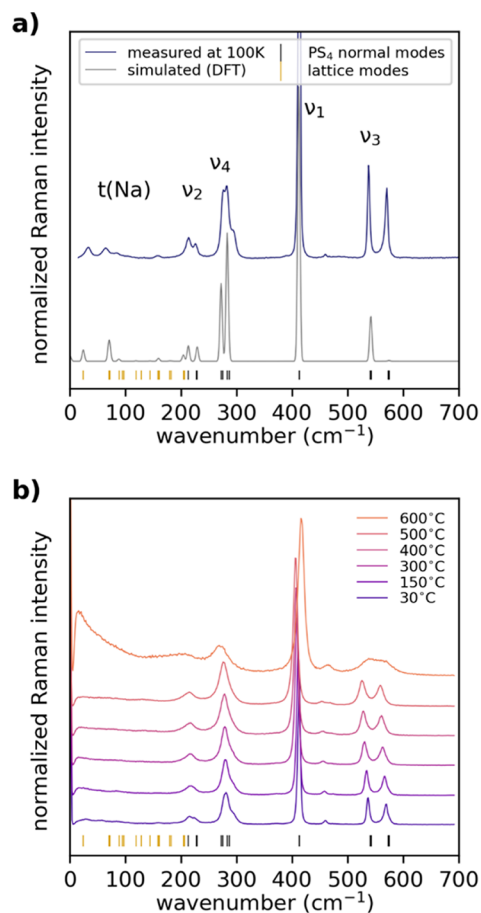


**Figure 3.** Raman spectra of  $\text{Na}_3\text{PS}_4$ . (a) Comparison of the experimental spectrum measured at 100 K and simulated based on DFT. The peak shape of the calculated spectrum is arbitrary.  $\nu_1$ – $\nu_4$  denotes the normal modes of the  $\text{PS}_4^{3-}$  tetrahedron: symmetric stretching, symmetric bending, asymmetric stretching, and asymmetric bending, respectively.  $t(\text{Na})$  represents modes associated with  $\text{Na}^+$  translation (b) evolution of the experimental Raman spectra with temperature in the range 30–600 °C.

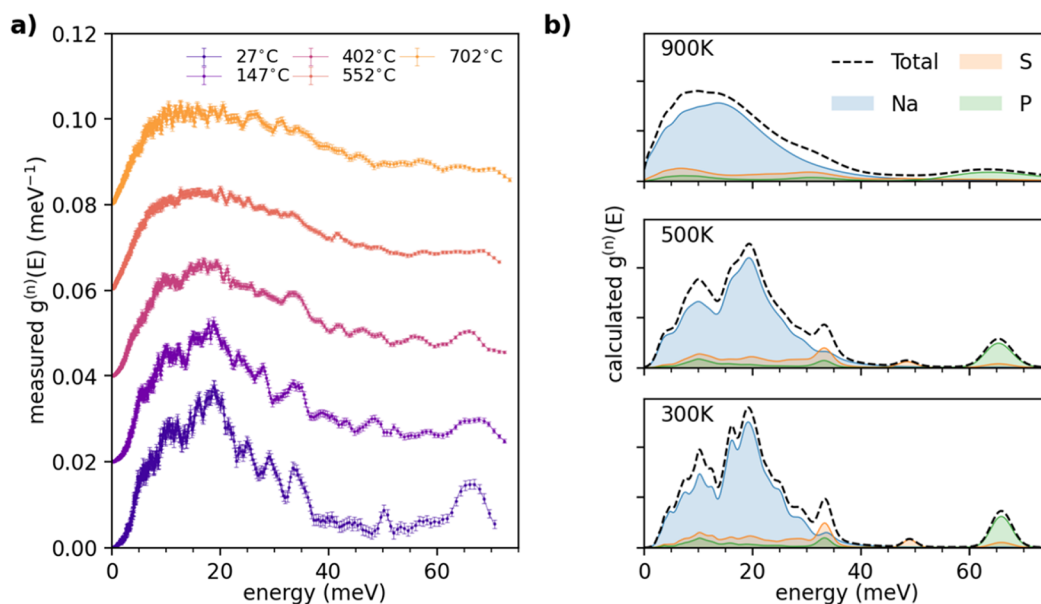


**Figure 4.** Neutron-weighted phonon density of states  $g^{(n)}(E)$  as (a) experimentally measured by INS and (b) extracted from AIMD calculations. Spectra in (a) staggered by  $0.02 \text{ meV}^{-1}$  for clarity.

**Table 1. Molecular Site Group Analysis for the  $\text{PS}_4^{3-}$  Anion in  $\alpha\text{-Na}_3\text{PS}_4$  and  $\beta\text{-Na}_3\text{PS}_4$ <sup>a</sup>**

$\alpha\text{-Na}_3\text{PS}_4$ ( $P\bar{4}2_1c$ )		
free ion symmetry	site symmetry	unit cell symmetry
$\bar{4}3m$ ( $T_d$ )	$\bar{4}$ ( $S_4$ )	$\bar{4}2m$ ( $D_{2d}$ )
$A_1$ ( $\nu_1$ )	$\rightarrow$ 3A	$\rightarrow$ $3A_1$ ( $\nu_1, \nu_2, r$ ) $3A_2$ ( $\nu_1, \nu_2, r$ )
$E$ ( $\nu_2$ )	$\rightarrow$ 4B	$\rightarrow$ $4B_1$ ( $\nu_2, \nu_3, \nu_4, t$ ) $4B_2$ ( $\nu_2, \nu_3, \nu_4, t$ )
$T_1$ ( $r$ )	$\rightarrow$ 4E	$\rightarrow$ 8E ( $2\nu_3, 2\nu_4, 2t, 2r$ )
$T_2$ ( $\nu_3, \nu_4, t$ )	$\rightarrow$ 4E	$\rightarrow$ 8E ( $2\nu_3, 2\nu_4, 2t, 2r$ )
$\beta\text{-Na}_3\text{PS}_4$ ( $I\bar{4}3m$ )		
free ion symmetry	site symmetry	unit cell symmetry
$\bar{4}3m$ ( $T_d$ )	$\bar{4}3m$ ( $T_d$ )	$\bar{4}3m$ ( $T_d$ )
$A_1$ ( $\nu_1$ )	$\rightarrow$ $A_1$	$\rightarrow$ $A_1$ ( $\nu_1$ )
$E$ ( $\nu_2$ )	$\rightarrow$ E	$\rightarrow$ E ( $\nu_2$ )
$T_1$ ( $r$ )	$\rightarrow$ $T_1$	$\rightarrow$ $T_1$ ( $r$ )
$T_2$ ( $\nu_3, \nu_4, t$ )	$\rightarrow$ $T_2$	$\rightarrow$ $T_2$ ( $\nu_3, \nu_4, t$ )

<sup>a</sup>Arrows indicate correlations between the symmetry of the free  $\text{PS}_4^{3-}$  anion, the point group symmetry of the P atom site (site group), and the point group of the unit cell (factor group).  $\nu_1$ – $\nu_4$ : normal modes, r: rotation/libration, t: translation.

that the ion diffusion pathways in the  $\text{Na}_3\text{PS}_4$  structure run parallel to the principal axes, phonons that displace  $\text{Na}^+$  along a, b, or c (#4–30 in Table 2) will have a direct influence on macroscopic ion diffusion, that is, these same lower-energy phonons are responsible for carrying the  $\text{Na}^+$  ions to the transition states for hopping to occur. Unfortunately, limitations of our experimental setup do not allow us to observe these said modes above RT (Figure 3b). The complete list of vibrational modes including their associated symmetries and comparison with experiment is tabulated in Table 2 for  $\alpha\text{-Na}_3\text{PS}_4$ , with details and the analogous analysis for  $\beta\text{-Na}_3\text{PS}_4$  shown in the Supporting Information (Tables S6–S12).

At RT and above, only the normal modes of the  $\text{PS}_4^{3-}$  are observable in the Raman spectra (Figure 3b). These evolve smoothly with heating, namely, softening (i.e., red shifting to

lower energies/wavenumbers) up to  $\sim 550$  °C. Most interestingly, the splitting of the  $\nu_3$  normal modes ( $\sim 550 \text{ cm}^{-1}$ ) that should be absent in the cubic description (Table 1) is observed invariantly in the temperature domain of the  $\beta$ -polymorph (250–500 °C), indicating that the local symmetry remains tetragonal and that the cubic average symmetry from Bragg diffraction does not accurately capture the local structure of  $\beta\text{-Na}_3\text{PS}_4$ . Above 550 °C, a distinct broadening of the peaks is observed along with discontinuous shifts in frequency: softening (red shift) of the  $\nu_2$  and  $\nu_4$  bending modes ( $\sim 210$  and  $270 \text{ cm}^{-1}$ ) corresponding to the intramolecular S–S repulsion and hardening (blue shift to higher energies/wavenumbers) of the  $\nu_1$  and  $\nu_3$  stretching modes ( $\sim 415$  and  $550 \text{ cm}^{-1}$ ) corresponding to the P–S covalent bond. The discontinuous peak shifts at  $\sim 550$  °C are accompanied by a distinct rise of the signal around the elastic peak ( $E = 0$ ). This “broadening of the elastic peak” points to a finite energy process of quasi-elastic nature and can be attributed to atomic mobility of continuous stochastic, nonphonon character (in contrast to discrete lattice excitations). These observations are reversible with hysteresis on cooling and assigned to the  $\beta$ -to- $\gamma$  phase transition. We note that blue shifting of molecular internal frequencies, as observed here for the P–S stretching modes, is typically characteristic of melting, consistent with the assignment of  $\gamma\text{-Na}_3\text{PS}_4$  as a “partially molten” mesophase.<sup>46</sup>

Figure 4a presents the phonon generalized density of states (GDOS) of  $\text{Na}_3\text{PS}_4$  extracted from INS measurements. The GDOS are complementary to the Raman spectra in that they involve a weighting of the scattering ions with their scattering power resulting, in the case of  $\text{Na}_3\text{PS}_4$ , in increased sensitivity for the lower energy modes involving  $\text{Na}^+$ . We note that both techniques probe the phonon spectrum: Raman spectroscopy probes uniquely the  $\Gamma$ -point (momentum  $q = 0$ ), while INS allows the probing of the whole Brillouin zone (function of  $q$ ).

The GDOS evolve significantly with temperature with features broadening significantly from RT to 400 °C. The spectra at 550 and 700 °C corresponding to the  $\gamma$ -phase show barely any features. Notably, the low energy (0–5 meV) behavior of the GDOS also significantly changes upon

**Table 2. Full List of Vibrational Modes of  $\alpha$ -Na<sub>3</sub>PS<sub>4</sub> Including Assignments Compared with the Modes Observable by Raman Spectroscopy at 100 K<sup>a</sup>**

$\alpha$ -Na <sub>3</sub> PS <sub>4</sub> ( $P\bar{4}2_1c$ )				
mode #	calc. freq (cm <sup>-1</sup> )	mode symmetry	exp. freq. (cm <sup>-1</sup> )	mode assignment
1	0	B2	acoustic	t(PS <sub>4</sub> , Na1, Na2   [001])
2–3	0	2xE	acoustic	t(PS <sub>4</sub> , Na1, Na2   [100], [010])
4–5	24	2xE	32	t(Na2   [100], [010]), r(PS <sub>4</sub>   [100], [010])
6	70	A1	70	t(Na1   [001]), r(PS <sub>4</sub>   [001])
7–8	72	2xE	84?	t(Na2   [100], [010])
9	88	B2	84?	t(Na1   [001])
10–11	94	2xE	not observed	t(PS <sub>4</sub>   [100], [010])
12	97	B1	not observed	t(PS <sub>4</sub>   [001])
13–14	119	2xE	not observed	r(PS <sub>4</sub>   [100], [010]), t(Na2   [100], [010])
15	128	(A2)	(inactive)	r(PS <sub>4</sub>   [001]), t(Na1   [001])
16–17	128	2xE	not observed	r(PS <sub>4</sub>   [100], [010]), t(Na2 [100], [010])
18	144	A1	not observed	r(PS <sub>4</sub>   [001]), t(Na1   [001])
19–20	158	2xE	not observed	t(Na1, Na2   [110]), r(PS <sub>4</sub>   [100], [010])
21–22	159	2xE	157?	t(Na2   [100], [010])
23	161	B1	157?	t(Na1   [001])
24	174	(A2)	(inactive)	t(Na1   [001]), r(PS <sub>4</sub>   [001])
25	179	B2	not observed	t(Na2   [001])
26	182	B1	not observed	t(Na2   [001])
27–28	204	2xE	not observed	t(Na1   [100], [010])
29–30	206	2xE	not observed	t(Na1   [110])
31–32	213	A1 (+ A2)	214	$\nu_2$ (PS <sub>4</sub> ) symmetric bending
33	227	B2	226	$\nu_2$ (PS <sub>4</sub> ) symmetric bending
34	229	B1	226	$\nu_2$ (PS <sub>4</sub> ) symmetric bending
35	272	B2	276	$\nu_4$ (PS <sub>4</sub> ) asymmetric bending
36	275	B1	276	$\nu_4$ (PS <sub>4</sub> ) asymmetric bending
37–38	283	2xE	283	$\nu_4$ (PS <sub>4</sub> ) asymmetric bending
39–40	287	2xE	293	$\nu_4$ (PS <sub>4</sub> ) asymmetric bending
41–42	412	A1 (+ A2)	413	$\nu_1$ (PS <sub>4</sub> ) symmetric stretching
43	541	B2	537	$\nu_3$ (PS <sub>4</sub> ) asymmetric stretching
44–45	542	2xE	537	$\nu_3$ (PS <sub>4</sub> ) asymmetric stretching
46	573	B1	567	$\nu_3$ (PS <sub>4</sub> ) asymmetric stretching
47–48	575	2xE	570	$\nu_3$ (PS <sub>4</sub> ) asymmetric stretching

<sup>a</sup> $\nu_1$ – $\nu_4$ : normal modes, r: rotation/libration, t: translation. For example, r(PS<sub>4</sub> | [001]) rotation of PS<sub>4</sub> about the *c*-axis; t(Na1 | [100],[010]) translation of Na1 along the *a*- and *b*-axes. Modes assigned according to the dominant atomic displacement vectors. Lattice modes (#1–30) sometimes include a secondary displacement in addition to the main one.

transition to  $\gamma$ -Na<sub>3</sub>PS<sub>4</sub>. Toward the transition to  $\gamma$ -Na<sub>3</sub>PS<sub>4</sub>, the Debye growth in the 0–5 meV acoustic region exhibits a clear deviation from a  $E^2$ -like behavior, possibly reflecting the onset of an amorphous or liquid-like structural component of the molten sublattices. The observed significant broadening of GDOS features with increasing temperature supports this interpretation and can also be considered as a consequence of increased amplitudes of atomic vibrations.

To interpret the measured spectra, we have extracted the neutron-weighted phonon density of states (GDOS) from the trajectories of *ab initio* molecular dynamics (AIMD) simulations of Na<sub>3</sub>PS<sub>4</sub> at 300, 500, and 900 K, representing the  $\alpha$ -,  $\beta$ -, and  $\gamma$ -polymorphs, respectively (Figure 4b). The agreement between the measured and calculated GDOS is excellent, and as such, we use it as a basis to interpret the evolution of the measured spectra with temperature. The phonon spectrum below  $\sim$ 30 meV is dominated by Na and shows distinct broadening with increasing temperature. While modes dominated by Na are well resolved for  $\alpha$ -Na<sub>3</sub>PS<sub>4</sub>, they start to broaden upon transition to the  $\beta$ -phase. The mode definition is lost completely upon transition to the  $\gamma$ -phase, and the average Na phonon energy sharply falls by around  $\sim$ 1 meV

(Supporting Information Figure S9). The reduction in average vibrational energy can be interpreted as softer interaction of Na with the anionic lattice.<sup>51</sup> The reduction in intensity and definition (damping) of the Na modes can be attributed to Na atoms no longer performing oscillatory motions but rather exhibiting long-range diffusion, that is, the Na-dynamics are no longer phonon-like but rather stochastic in nature. Similar arguments can be made for the PS<sub>4</sub><sup>3-</sup> tetrahedra which do not vibrate in unison but rather undergo individual stochastic rotations. The  $\gamma$ -phase is therefore dynamically dominated by uncorrelated motions, akin to a liquid. This interpretation is supported by the observation of a characteristic quasi-elastic signal which will be discussed independently in a forthcoming contribution focused on quasi-elastic neutron scattering.

**Thermal Analysis.** The thermogram of Na<sub>3</sub>PS<sub>4</sub> on heating, shown in Figure 5, reveals a single endothermic effect in the range 30–600 °C, with an onset at  $\sim$ 500 °C, in agreement with previous measurements.<sup>46,47</sup> Here, we performed differential scanning calorimetry (DSC), calibrated with a standard reference so that the isobaric heat capacity ( $c_p$ ) could be quantified. The  $c_p$  was determined to be  $\sim$ 1.0 J g<sup>-1</sup> K<sup>-1</sup> in the range 30–500 °C and  $\sim$ 1.2 J g<sup>-1</sup> K<sup>-1</sup> for temperatures  $>$ 520

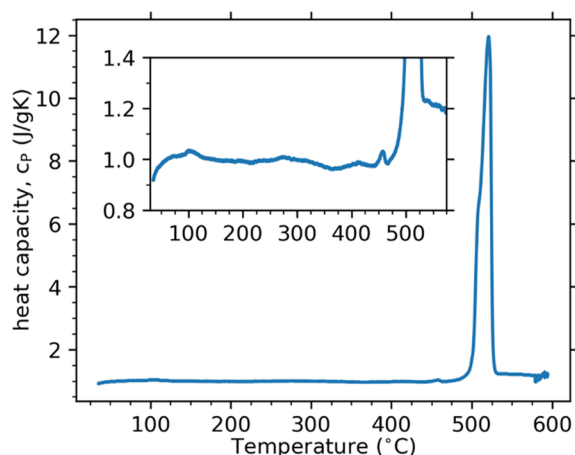


**Figure 5.** Thermogram of  $\text{Na}_3\text{PS}_4$  on heating in the range 30–600 °C from DSC. Inset: Magnification of the  $y$ -axis showing an increase in the baseline above 500 °C.

°C. The small endothermic peak observed at  $\sim 460$  °C is not observed in other DSC runs and thus likely constitutes an experimental artifact. Additional DSC experiments were performed using quartz crucibles to avoid reaction with  $\text{Na}_3\text{PS}_4$  and allow for thermograms up to 800 °C, exhibiting the onset of a large endothermic effect at 765 °C (Figure S11). In parallel, pelletized samples were evacuated in quartz ampoules and heated to various temperatures for visual inspection (Figure S12). From these experiments, we determine the melting point of  $\text{Na}_3\text{PS}_4$  as 765 °C in contrast to the previously cited value of 517 °C,<sup>47,52</sup> which actually pertains to the  $\beta$ -to- $\gamma$  phase transition.<sup>46</sup>

## DISCUSSION

In the following, we use our comprehensive variable-temperature data to classify the phase transitions in  $\text{Na}_3\text{PS}_4$  and discuss the nature of the high-temperature polymorphs  $\beta$  and  $\gamma$ .

**Classification of Phase Transitions.** By definition, the Gibbs free energies,  $G$ , of two polymorphs are equal at the phase transition temperature ( $\Delta G_{\text{trans}} = 0$ ). However, the derivatives of  $G$  might show discontinuities and phase transitions can be classified with respect to such discontinuities (Ehrenfest classification<sup>53</sup>). Discontinuities in the first derivative of  $G$ , that is, entropy ( $S = (\partial G/\partial T)_P$ ) or volume ( $V = (\partial G/\partial P)_T$ ), characterize “first-order” phase transitions. At the phase transition temperature  $\Delta G_{\text{trans}} = 0$  and  $\Delta H_{\text{trans}} = \Delta S_{\text{trans}}/T$ , so changes in entropy in first-order transitions typically manifest in a latent heat ( $\Delta H$ ) observable in thermal analysis. Similarly, discontinuities in the second derivative of  $G$ , that is, isobaric heat capacity ( $c_p = T(\partial S/\partial T)_P \propto d^2G/dT^2$ ), thermal expansion coefficient ( $\alpha_V = 1/V(\partial V/\partial T)_P \propto d^2G/dP dT$ ), and isothermal compressibility ( $\beta_T = -1/V(\partial V/\partial P)_T \propto d^2G/dP^2$ ), denote “second-order” phase transitions and so on.

**$\alpha$ -to- $\beta$  Phase Transition.** As evident from the thermogram of Figure 5, there is no discernible latent heat associated with the  $\alpha$ -to- $\beta$  phase transition in  $\text{Na}_3\text{PS}_4$ , nor a discontinuity in heat capacity. Under the heating rate of 5 °C/min utilized in our X-ray Bragg diffraction experiment, a large temperature range of coexistence for the  $\alpha$ - and  $\beta$  polymorphs can be observed, spanning roughly 180–280 °C (Figure S13). It is unclear at this point whether this coexistence is due to kinetic effects due to the rapid heating rate or whether a temperature

region of thermodynamic equilibrium exists for the two-phase mixture. No discontinuity in volume is observed, but a slight discontinuity in the thermal expansion coefficient is detected (Figure 1b, inset). The PDFs and Raman spectra exhibit a smooth evolution in this range of temperatures, indicating no stark change in local structure (Figures 2 and 3b, respectively).

Figure 6 schematically depicts the slight structural differences in the structures of the  $\alpha$  and  $\beta$ -polymorphs of  $\text{Na}_3\text{PS}_4$ . A

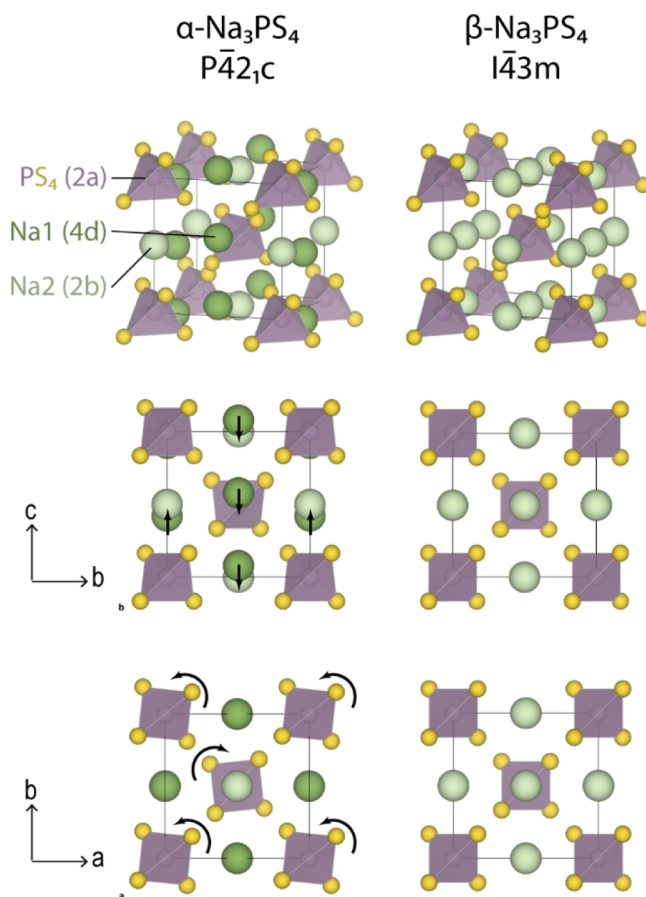


**Figure 6.** Structural relationship between  $\alpha$  and  $\beta$ - $\text{Na}_3\text{PS}_4$ . The transition occurs upon translation of the 4d Na1 atoms (highlighted in brown) and rotation of the  $\text{PS}_4$  tetrahedra about the  $c$ -axis. These atomic displacements are associated with the soft mode observable at  $70\text{ cm}^{-1}$  in the Raman spectra. The model for the  $\beta$ -phase shown here includes a single Na atom at the 6b position for simplicity, in contrast to the 1/4-occupied 24f site that results in slightly better fits of the Bragg diffractograms.

close group–subgroup relationship exists between the space groups of the two polymorphs,  $P421c$  and  $I43m$ , as shown in Table 3. We note that an intermediate body-centered tetragonal group, namely,  $I42m$ , is predicted by crystallographic theory,<sup>54</sup> which, however, we were not able to unambiguously identify in our experiments. For the  $\alpha$ -to- $\beta$  transition to occur, it is necessary for Na atoms to translate and for the  $\text{PS}_4$  units to slightly rotate. Namely, the 4d Na atoms in  $\alpha$ - $\text{Na}_3\text{PS}_4$  need to slide along the  $c$ -axis, so that their  $z \sim 0$  (see Table 3 and Figures S14–S15). The  $\text{PS}_4$  rotation also happens about the  $c$ -axis, that is, the S atoms coherently shift in the  $ab$  plane (Figure S16). Through these subtle translations and the convergence of the lattice parameters (Figure S14), the average symmetry is increased from tetragonal to cubic upon heating.

Table 3. Group–Subgroup Relationship of the Different Atomic Positions in the  $\alpha$ - and  $\beta$ -Polymorphs of  $\text{Na}_3\text{PS}_4$ <sup>a</sup>

atom	$\alpha$ - $\text{Na}_3\text{PS}_4$ , $P\bar{4}2_1c$ (114)		$\bar{I}42m$ (121)		$\beta$ - $\text{Na}_3\text{PS}_4$ , $\bar{I}43m$ (217)	
	Wyckoff	point grp.	Wyckoff	point grp.	Wyckoff	point grp.
P	2a (0, 0, 0)	$\bar{4}$	2a (0, 0, 0)	$\bar{4}2m$	2a (0, 0, 0)	$\bar{4}3m$
S	8e (x, y, z)	1	8i (x, x, z)	$\dots m$	8c (x, x, x)	$\dots 3m$
Na1	4d (0, 1/2, z)	2	4c (0, 1/2, 0)	222	6b (0, 1/2, 1/2)	$\bar{4}2m$
Na2	2b (0, 0, 1/2)	$\bar{4}$	2b (0, 0, 1/2)	$\bar{4}2m$		
(Na3)			8g <sub>1</sub> (x <sub>1</sub> , 0, 1/2)	$\dots 2.$		
			8g <sub>2</sub> (x <sub>2</sub> , 0, 1/2)	$\dots 2.$	24f (x, 1/2, 0)	$\dots 2.$
			8h (0, 1/2, z)	$\dots 2..$		

<sup>a</sup>25% occupied Na3 offers an alternative description to Na1 + Na2 for  $\beta$ - $\text{Na}_3\text{PS}_4$ .

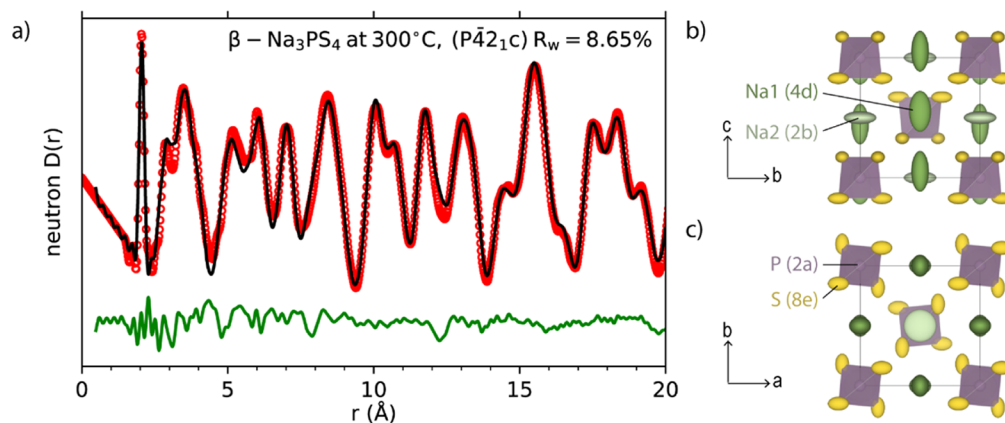


**Figure 7.** Neutron PDF of  $\text{Na}_3\text{PS}_4$  at 300 °C. (a) Small-box Rietveld-type fit to the data in the range 0.5–20 Å in the tetragonal  $P\bar{4}2_1c$  space group. (b,c) Visualizations of the refined structure projected in the  $bc$  and  $ab$  planes, respectively. Ellipsoids drawn at 75% probability. The displacements of Na1 and S correspond exactly to the  $\alpha$ -to- $\beta$  phase transition in  $\text{Na}_3\text{PS}_4$ .

We underline that these exact atomic displacements associated with the  $\alpha$ -to- $\beta$  phase transition constitute a specific vibrational mode at the  $\Gamma$ -point: mode #6 in Table 2, observable at 70  $\text{cm}^{-1}$  in the Raman spectra of Figure 3a; however, the limited sensitivity of our Raman measurements do not allow us to track the evolution of this mode around the  $\alpha$ -to- $\beta$  transition temperature. Furthermore, model calculations of the Raman spectra of the  $\beta$ -polymorph ( $\bar{I}43m$ ) in the conventional setting (two formula units) result in a shift of this mode to negative (unphysical) frequencies, confirming the dynamic instability of the  $\beta$ -polymorph at 0 K.<sup>c</sup>

From the ensemble of these observations, namely, no discontinuity in the first derivatives of free energy ( $V$ ,  $S$ ) and a slight discontinuity in the second derivative ( $\alpha_V$ ), we characterize the  $\alpha$ -to- $\beta$  transition in  $\text{Na}_3\text{PS}_4$  as one of weak second-order. Furthermore, given that the atomic displacements of Na and S are responsible for the transition (Figure 6), we characterize it as displacive.<sup>d</sup> We note that previous theoretical work has shown that the  $\alpha$ -to- $\beta$  transition can also be brought about by applied pressure, which is consistent with the lower lattice volume exhibited by  $\beta$ - $\text{Na}_3\text{PS}_4$  stabilized at RT through mechanochemistry.<sup>45</sup> Thus, overall, increasing temperature and increasing pressure both favor the higher-average-symmetry  $\beta$ -phase.

It is then of interest to discuss the nature of the  $\beta$ -phase, especially in view of practical applications as it had been shown that this medium-temperature phase could be stabilized under ambient conditions by mechanochemistry, reportedly resulting in elevated  $\text{Na}^+$  conductivity compared to the  $\alpha$ -phase.<sup>5,6</sup> We have thoroughly examined these mechanochemical effects in

an earlier contribution where we in fact detected no significant differences in the local structure between the ball-milled- and high-temperature-synthesized samples; they both present tetragonal local symmetry.<sup>45</sup> Further, it is our interpretation that the higher reported ionic conductivity of ball-milled samples is due to microstructural effects, namely, facile consolidation into the millimeter-scale pellets utilized for impedance spectroscopy measurements.<sup>45</sup>

In considering a well-crystallized sample of  $\beta$ - $\text{Na}_3\text{PS}_4$  at 300 °C in the present study, similar observations can be made: in contrast to the apparently cubic average structure, the local structure experimentally observed by the PDF can be better described in small-box, Rietveld-type simulations in the tetragonal  $P\bar{4}2_1c$  space group, indicating a tetragonal local structure similar to the RT  $\alpha$ -phase. The Raman spectra show no discontinuity upon transition to the  $\beta$ -phase, and the splitting of normal modes associated with the tetragonal distortion persists, showing no indication of a more symmetric environment for the  $\text{PS}_4^{3-}$  polyanions, as implied by the cubic description. In fact, neither static nor dynamic effects could result in observable Raman peak splitting (i.e., lifting of degeneracy) in a local environment truly exhibiting  $\bar{I}43m$ , as can be seen in molecular site group analysis of Table 1 and discussed in detail in the Supporting Information.<sup>49</sup> The only concrete evidence of a phase transition stems from Bragg diffraction, where a convergence of the lattice parameters to a cubic cell is clearly observed.

This set of observations leads us to describe  $\beta$ - $\text{Na}_3\text{PS}_4$  as a “pseudocubic” polymorph, closely related to the tetragonal ground-state  $\alpha$ - $\text{Na}_3\text{PS}_4$ . We hypothesize that these seemingly

contrasting observations can be reconciled by an increased atomic mobility in  $\beta$ - $\text{Na}_3\text{PS}_4$ , namely, translational for the  $\text{Na}^+$  and rotational for the  $\text{PS}_4^{3-}$ . In the cubic long-range framework, such atomic mobility can lead to localized tetragonal distortions which could explain the PDF and Raman spectroscopic findings, as previously hypothesized in relation to room-temperature-stabilized samples of  $\beta$ - $\text{Na}_3\text{PS}_4$ .<sup>8,45,55</sup> Such tetragonal distortions are exactly the displacements (translations and rotations) shown in Figure 6 and could be static or dynamic in nature, the differentiation between which should be the subject of further study. It is likely that the distribution of such tetragonal domains within crystallites of  $\beta$ - $\text{Na}_3\text{PS}_4$  dynamically evolves at high temperatures (250–500 °C) and “frozen” for samples stabilized at RT, for example, by mechanochemistry or quenching. The tetragonal distortions can manifest locally with the same probability along any of the three principal axes of the  $\beta$ - $\text{Na}_3\text{PS}_4$  unit cell, leading to the structure appearing cubic on the average scale. This interpretation, is supported by the refinement of the neutron PDF recorded at 300 °C, as shown in Figure 7a. The refined anisotropic displacement parameters for Na and S, visualized in Figure 7b,c, show direct evidence of the atomic translations associated with the tetragonal distortion in Figure 6, namely, along the  $c$  axis for Na and in the  $ab$  plane for S.

These observations on the nature of the  $\beta$ -polymorph of  $\text{Na}_3\text{PS}_4$  likely also apply to the isostructural  $\text{Na}_3\text{PnX}_4$  (Pn: P, As, Sb; X: S, Se), which all exhibit analogous  $\alpha$ - $\beta$  polymorphism. The selenides  $\text{Na}_3\text{PSe}_4$  and  $\text{Na}_3\text{SbSe}_4$  actually exhibit the  $\beta$ -phase at ambient temperature (their corresponding  $\alpha$ -to- $\beta$  transition temperatures are approximately –30 and –80 °C, respectively<sup>16</sup>). Indeed, the Raman spectra of the  $\beta$ -polymorphs of  $\text{Na}_3\text{PSe}_4$  and  $\text{Na}_3\text{SbSe}_4$  show the same signs of tetragonal local structure through splitting of the  $\nu_3$  modes,<sup>16,24,51</sup> as shown here for  $\text{Na}_3\text{PS}_4$ .

**$\beta$ -to- $\gamma$  Phase Transition.** The high-temperature  $\gamma$ -phase is indexed in the space group  $Fddd$ , which bears no group-subgroup relationship with those of the two lower-temperature polymorphs. Although the  $\beta$ -phase continues to be observable in Bragg diffractograms in the range 500–540 °C, its lattice parameters cease to evolve in this temperature range. A large discontinuity in volume is observed, along with a discontinuity in the thermal expansion coefficient. In contrast to the  $\alpha$ -to- $\beta$  transition, the  $\beta$ -to- $\gamma$  is associated with a large latent heat of  $\sim 150$  J/g and a change in heat capacity from  $\sim 1.0$  to  $\sim 1.2$  J/(g K). In addition, since at the transition temperature  $\Delta G_{\text{trans}} = 0$ , we can estimate the entropy change of transition as  $\Delta S_{\text{trans}} = \Delta H_{\text{trans}}/T_{\text{trans}} = 0.19$  J/(g K). We note that the transition temperature varies significantly between experiments ( $\sim 550$  °C for Raman,  $\sim 470$  °C for PDF, and  $\sim 500$  °C for DSC and Bragg diffraction); we tentatively ascribe these discrepancies to the different temperature control setups, heating rates, and sample amounts inherent to the different techniques. A strong hysteresis of the transition temperature is observed in all experiments conducted on cooling (Bragg diffraction, Raman spectroscopy, and DSC).

From the ensemble of these observations, namely, strong discontinuities in the first derivatives of free energy ( $V$  and  $S$ ) and no structural relation to the lower-temperature polymorphs, we conclude that the  $\beta$ -to- $\gamma$  transition in  $\text{Na}_3\text{PS}_4$  is of reconstructive nature and thermodynamically of first-order character.

We have posited in a previous contribution that  $\gamma$ - $\text{Na}_3\text{PS}_4$  is a mesophasic material of plastic crystalline nature<sup>46</sup> and the additional data presented here support that description. The Raman spectra at high temperatures indicate isolated  $\text{PS}_4^{3-}$  tetrahedra in a liquid-like environment. Both the Raman and inelastic neutron spectra indicate the breakdown of phonon quasi-particles for Na-dominated modes in favor of stochastic, incoherent, “nonphonon-like” behavior, again indicative of a molten Na sublattice. The Lorentzian broadening of the central, elastic peaks in both these inelastic scattering techniques indicate fast diffusive behavior likely attributed to both the  $\text{Na}^+$  and  $\text{PS}_4^{3-}$  (translational and rotational, respectively).

Raman and neutron spectroscopies expose a discontinuous evolution of the P–S covalent bonds and the Na–S ionic interactions upon transition to the  $\gamma$ -phase. Namely, the P–S bond stiffens (Figure 8a) in contrast to the typical trends upon

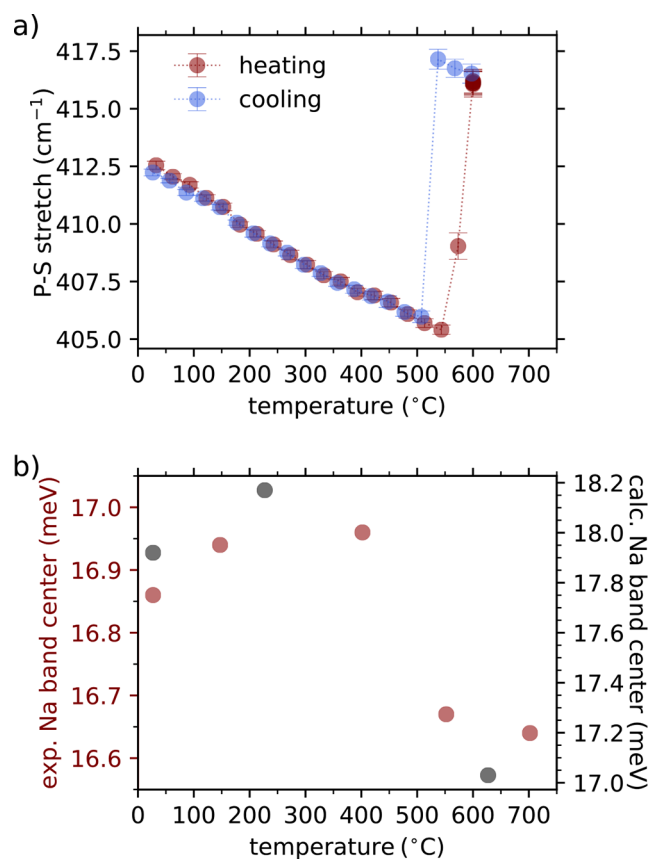


**Figure 8.** Evolution of the bonding in  $\text{Na}_3\text{PS}_4$  with temperature (a) evolution of the P–S stretching ( $\nu_1$ ) frequency from Raman spectroscopy (b) evolution of the average vibrational energy of Na from neutron spectroscopy and associated calculations.

heating of solid materials. This stiffening of the internal interaction in the  $\text{PS}_4^{3-}$  moiety is concomitant with a softening of the interaction between  $\text{PS}_4^{3-}$  and  $\text{Na}^+$ , as evident from the decreased average vibrational energy of sodium observed in the GDOS (Figure 8b). These effects could perhaps be interpreted as an instance of the so-called “inductive effect” as applied recently to solid electrolytes<sup>56,57</sup> brought about in this case by temperature-driven phase transformation rather than chemical substitution; that is to say, the electronic density around the sulfur atoms shifting from coordinating the  $\text{Na}^+$  ions to the P–

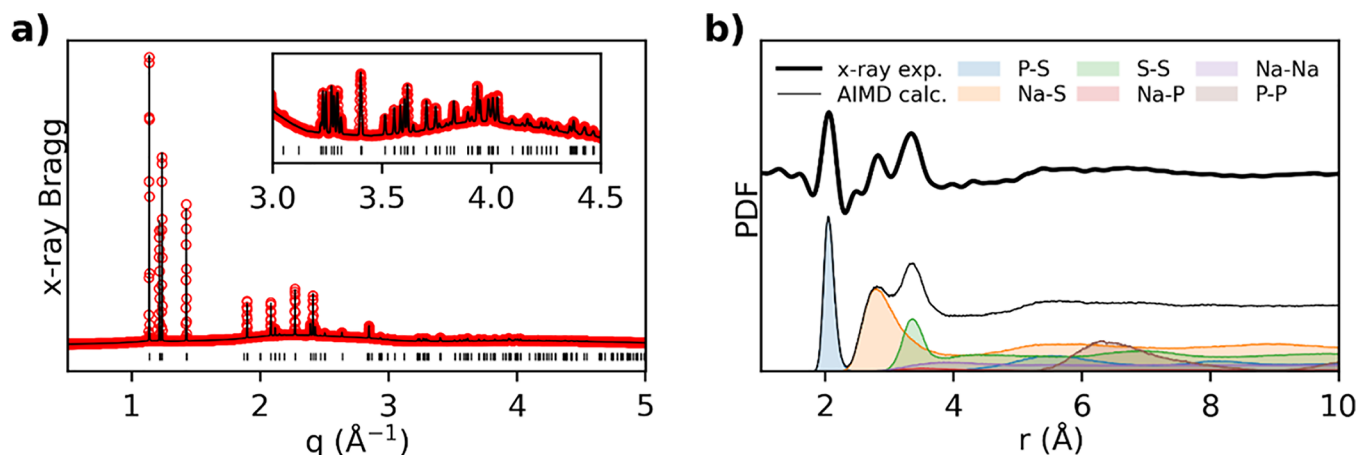


**Figure 9.** Diffraction analysis of  $\gamma$ - $\text{Na}_3\text{PS}_4$  (a) Bragg diffractogram at 550 °C indexed in the  $Fddd$  space group and (b) comparison of PDFs as experimentally measured using X-rays at 600 °C and extracted from AIMD simulations at 900 K.

S covalent bonds, rendering the P–S covalent bond stiffer and the Na–S ionic interaction softer. This interpretation would also be consistent with the concomitant step-wise softening of the bending modes observed in Raman upon transition to the  $\gamma$ -phase (Figure 3), corresponding to weaker S–S (coulombic) repulsion.

It is noted that, in terms of the P–S bond length as observed by PDF, no significant deviation is observed from the expected thermal expansion upon transition to the  $\gamma$ -phase (Figure S17). This observation would indicate no dramatic change in the chemical nature of the intramolecular P–S bond despite the observed stiffening and the presumed strengthening implied by the “inductive effect”. These preliminary observations on the evolution of the P–S and Na–S bonds should be verified and expanded on by more direct means in future work.

In addition, the PDF of  $\gamma$ - $\text{Na}_3\text{PS}_4$  indicates no strong interatomic correlations beyond the first neighbor P–S, Na–S and S–S pairs, reminiscent of amorphous or liquid systems. This might appear counter-intuitive, given the distinct Bragg reflections exhibited by  $\gamma$ - $\text{Na}_3\text{PS}_4$ , clearly indicating a macroscopically solid crystalline material (Figure 9a). We have verified these observations against our AIMD simulations published previously.<sup>46</sup> As shown in Figure 9b, the experimental and simulated PDFs are in excellent agreement. This same feature of a liquid-like PDF was also reported recently in independent classical molecular dynamics investigations of  $\gamma$ - $\text{Na}_3\text{PS}_4$  by Sau and Ikeshoji.<sup>58</sup>

The combination of sharp Bragg reflections (long-range order) and a flat PDF (no short-range correlations) might seem counter-intuitive, but is perfectly in-line with the plastic nature of the crystal and highlights the different information accessible by Bragg and total-scattering analyses.<sup>59</sup> The time-averaged centers of mass of the  $\text{PS}_4^{3-}$  and the Na probability density are arranged periodically and define the average motif that gives rise to long-range symmetry and Bragg reflections. The sharp P–S and S–S peaks in the PDF elucidate that the  $\text{PS}_4^{3-}$  moves as a rigid unit, that is, the material remains as an ionic molecular crystal of  $\text{Na}^+$  and  $\text{PS}_4^{3-}$ . At the same time, individual  $\text{PS}_4^{3-}$  tetrahedra can adopt a multitude of orientations, unconstrained by the orientation of their neighboring tetrahedra. This is captured in the PDF, where, for example, the second P–S neighbor and the first P–P neighbor distances between tetrahedra, nominally at  $\sim 5.5$  and  $\sim 6.5$  Å, respectively, are quite variable between different

instantaneous snapshots; consequently, the said peaks are remarkably broadened and not distinguishable in the total PDF. The distinct asymmetry in first Na–S peak at  $\sim 2.8$  Å indicates that Na is not so much “bonded” to the sulfur but rather sterically limited in its liquid-like diffusion by the position of sulfur, that is, it cannot approach closer than  $\sim 2.7$  Å. The Na–Na radial distribution function (RDF) is remarkably broad and featureless, indicating liquid-like distribution with no correlation. This feature of a liquid-like broad Na–Na radial distribution was also confirmed in the study of Sau and Ikeshoji<sup>58</sup> and is in direct contrast to sharp RDF peaks around 3.5 Å in the case of the  $\alpha$ - and  $\beta$ -polymorphs,<sup>32,60</sup> where Na is relatively constrained at fully occupied lattice sites.

Another interesting point to discuss relates to the apparent “symmetry lowering” upon the  $\beta$ -to- $\gamma$  phase transition. It is hard to quantify unambiguously the amount of symmetry between two space groups not related by group–subgroup relationships, as is the case here. Still, from the point of view of symmetry operations per cell volume, the orthorhombic  $Fddd$  is clearly of lower symmetry than the cubic  $I\bar{4}3m$ . Why would then a high-temperature, high-disorder polymorph exhibit lower symmetry?

It seems that the melting of the Na-ion sublattice destabilizes a bcc-like arrangement of  $\text{PS}_4^{3-}$  units, as found in the  $\alpha$ - and  $\beta$ -polymorphs, and the liquid-like Na-sublattice seems to dictate a more complex arrangement of the  $\text{PS}_4^{3-}$  anions, as exhibited in the larger orthorhombic cell of the  $\gamma$ -phase. Viewed from another perspective, it is possible that the higher volume required by the highly mobile Na sublattice cannot be accommodated in the body-centered cell; note that the first Na–Na RDF peak at  $\sim 3.5$  Å for the  $\alpha$ - and  $\beta$ -phases while  $\sim 4$  Å for the  $\gamma$ . It is noted that thermograms of the  $\text{Na}_3\text{PS}_4$ -isostructural  $\text{Na}_3\text{SbS}_4$ ,  $\text{Na}_3\text{PSe}_4$ , and  $\text{Na}_3\text{SbSe}_4$  (not shown here) do not indicate the presence of a  $\gamma$ -type plastic polymorph before melting. These isostructural compounds exhibit significantly larger lattice volumes compared to  $\text{Na}_3\text{PS}_4$ , which could be the reason why they can accommodate the increased mobility of Na up to the melting point without breaking the bcc-like arrangement of their respective tetrahedral polyanions.

To our knowledge, the case of  $\gamma$ - $\text{Na}_3\text{PS}_4$  is unique with respect to its crystal structure; most of the immediately comparable molecular crystal compounds characterized by

rotational disorder of their constituent tetrahedral polyanions exhibit full cubic symmetry  $Fm\bar{3}m$  (e.g.,  $\alpha$ -Li<sub>2</sub>SO<sub>4</sub>, ref 61;  $\gamma$ -Na<sub>3</sub>PO<sub>4</sub>, refs 62 and 63;  $\gamma$ -Na<sub>4</sub>Zn(PO<sub>4</sub>)<sub>2</sub>, ref 64;  $\alpha$ -NaBH<sub>4</sub>, refs 65 and 66). Nevertheless, an analogy can be found in the equally surprising observations of  $Fddd$  symmetry in the seemingly unrelated systems of block copolymer melts, that is, polymers of two or more different monomers arranged in a linear fashion along the polymer chain. These systems present a host of mesophases between their liquid and solid forms, and recently, self-assemblies of AB diblock<sup>67–71</sup> and ABC triblock<sup>72–74</sup> copolymer melts have been observed to exhibit the  $Fddd$  symmetry. Although these structures present the  $Fddd$  symmetry on a much larger scale (of the order of 10 nm; observable by small-angle scattering/diffraction) a number of similarities indicate a fundamental connection between them and  $\gamma$ -Na<sub>3</sub>PS<sub>4</sub>. Namely, theoretical and experimental analyses converge to the ideal ratio of orthorhombic unit cells of dimensions approaching  $a/b/c = 1:2:2\sqrt{3}$  ( $\approx 3.46$ ) for such mesophases, which is very close to what we observe for  $\gamma$ -Na<sub>3</sub>PS<sub>4</sub> (1:1.8:3.2). These systems are mesophasic, with properties in between solid and liquid, and exhibit remarkable mobility of their constituent atoms. In a recent theoretical investigation, it was shown that such  $Fddd$  mesophases could be stabilized even in single-component systems, in which case, the diffusivity of constituent particles was practically identical to that of the liquid phase.<sup>75</sup> These  $Fddd$  mesophases were shown to be stable at specific volume ratios between the different block copolymers or equivalently at a specific density for the single-component systems,<sup>75</sup> which by analogy lends weight to our hypothesis that steric considerations are the key parameter in the stability of  $\gamma$ -Na<sub>3</sub>PS<sub>4</sub>.

## CONCLUSIONS

We have reported here a thorough variable-temperature analysis of the Na-ion conductor Na<sub>3</sub>PS<sub>4</sub> through diffraction (Bragg and PDF), spectroscopy (Raman and INS), and associated DFT-based simulations. We demonstrate that such a multitechnique approach is critical for the accurate interpretation of often-contrasting observations regarding the polymorphs of Na<sub>3</sub>PS<sub>4</sub>. We have determined the thermal expansion coefficient ( $\sim 10^{-4}$  K<sup>-1</sup> at RT) and isobaric heat capacity ( $\sim 1.0$  J g<sup>-1</sup> K<sup>-1</sup>), as well as the melting point (765 °C) of Na<sub>3</sub>PS<sub>4</sub>. Our results converge in the characterization of the  $\alpha$ -to- $\beta$  transition at  $\sim 250$  °C as a weak second order, displacive phase transition and the  $\beta$ -to- $\gamma$  transition at  $\sim 500$  °C as a first-order, reconstructive phase transition. Our combined diffraction spectroscopy analysis indicates that the  $\beta$ -phase, although cubic on the average scale, is characterized by a tetragonal local structure through subtle displacements of the Na and S atoms. These said displacements are likely dynamic at high temperature and static when stabilized around RT. The  $\gamma$ -polymorph is shown to be mesophasic, with properties between solid and liquid, combining strong Bragg diffraction and a featureless PDF. Transition to the  $\gamma$ -phase seems to involve a distinct change in bonding, namely, stiffening of the covalent intramolecular bonds of the PS<sub>4</sub><sup>3-</sup> unit and softening of the ionic interaction between Na<sup>+</sup> and the anionic species.

This detailed study has shed new light on the rich polymorphism of Na<sub>3</sub>PS<sub>4</sub>, which is relevant to its potential use in sodium-based solid-state batteries.

## METHODS

**Synthesis.** Na<sub>3</sub>PS<sub>4</sub> was synthesized by a solid-state synthesis route as first reported by Jansen and Henseler.<sup>47</sup> Stoichiometric ratios of the binary reagents Na<sub>2</sub>S and P<sub>2</sub>S<sub>5</sub> (Sigma-Aldrich, utilized as received) were intimately mixed first in a mortar pestle and then in a ball-mill jar (typically 5 g of precursors with 25 10 mm ZrO<sub>2</sub> balls in an 80 mL ZrO<sub>2</sub> jar, milled for 12 h at 500 rpm). The resulting powder was pelletized and placed in carbon-coated quartz tubes. The carbon coating of the tubes was achieved by acetone pyrolysis and subsequent annealing at 1000 °C for 12 h under Ar. The quartz tubes were then flame-sealed under vacuum ( $\sim 10^{-2}$  mbar) and placed in a furnace for reaction. The temperature of the furnace was slowly increased to 500 °C at 1 °C/min, held for 20 h, and naturally cooled to RT. The products after synthesis were milled by pestle and mortar into fine powders for further analysis. All handling was performed in Ar-filled gloveboxes.

**Bragg Diffraction.** X-ray powder Bragg diffraction experiments were performed at the BL04-MSPD beamline<sup>76,77</sup> of the ALBA synchrotron in Barcelona, Spain. The samples were flame-sealed in Ar-filled 1 mm-diameter quartz capillaries. Diffractograms were collected in transmission geometry, using the position-sensitive detector MYTHEN and a wavelength of 0.8262 Å, selected using a Si 111 reflection double crystal monochromator. The temperature of the sample was controlled using a hot air blower, calibrated using the thermal expansion of a standard Si sample. Short measurements (30 s) were continuously recorded on heating and cooling from RT to 550 °C and back, at a rate of 5 °/min. Longer measurements (270 s) were taken at 30, 300, 500, and 550 °C for refinement.

Neutron powder Bragg diffraction experiments were performed at the D2B beamline of the Institut Laue-Langevin (ILL) in Grenoble, France. The samples ( $\sim 2$  g) were sealed in cylindrical vanadium containers, which were then put inside a vacuum furnace connected to a secondary pump ( $\sim 10^{-5}$  mbar). Diffractograms were collected in transmission geometry, using 128 <sup>3</sup>He counting tubes and a wavelength of 1.594 Å selected using the (335) reflection of Ge[115] monochromators. Measurements of  $\sim 4$ –6 h were taken at 30 and 300 °C.

The analysis of the Bragg diffraction data was performed using the programs in the Fullprof and Jana 2006 software suites.<sup>78,79</sup> The background was defined as a linear interpolation between manually selected points. Le Bail fits were performed to describe the peak broadening using the Thompson–Cox–Hastings pseudo-Voigt function<sup>80</sup> (convoluted with the instrumental resolution in the case of X-rays). In subsequent Rietveld analyses, occupancies were fixed to the Na<sub>3</sub>PS<sub>4</sub> stoichiometry, and atomic positions and displacement parameters were fitted.

**Total Scattering.** X-ray total scattering experiments were performed at the 11-ID-B beamline of the Advanced Photon Source at the Argonne National Laboratory using high-energy X-rays ( $\lambda = 0.21130$  Å) for high values of momentum transfer ( $Q = 24.5$  Å<sup>-1</sup>). Samples were flame-sealed under Ar in quartz capillaries. The temperature of the sample during measurement was controlled using a hot-air blower. One-dimensional diffraction data were obtained by integrating the raw 2D total scattering data in Fit2D. PDFs were extracted from the background- and Compton scattering-corrected data following Fourier transform using PDFgetX2.<sup>81</sup>

Neutron total scattering experiments were performed at the POLARIS beamline of the ISIS neutron source. The powder samples ( $\sim 2.5$  g) were loaded into cylindrical vanadium containers and sealed using copper rings under Ar in a glovebox, which were then put inside a vacuum furnace connected to a secondary pump. Measurements were taken at 30, 300, and 600 °C for 8, 8, and 10 h, respectively. The total scattering data were normalized, corrected for nonsample scattering, and Fourier-transformed to produce PDFs using the program GudrunN.<sup>82</sup>

The analysis of the neutron PDFs at 30 and 300 °C was performed using the PDFfit2 engine, as implemented in PDFgui.<sup>81</sup> Structural refinements were limited to single unit cells (no supercells) and constrained by the space group symmetry observed in Bragg

diffraction ( $P4_21c$  or  $I43m$ ). The following parameters were refined in this order: (1) scale factor, (2) peak broadening parameter with  $1/r$  dependence,  $\delta 1$  (3) lattice parameters, (4) atomic positions, and (5) thermal displacement parameters. The instrumental resolution parameters  $Q_{\text{damp}}$  and  $Q_{\text{broad}}$  were set at 0.01 and 0.03, respectively, as determined from measurement of a silicon standard.

The quality of each refinement is quantified by the reliability factor weighted  $R$ -value,  $R_w$ , which describes the difference between the experimental data (obs) and the fit (calc) each data point

$$R_w = \sqrt{\frac{\sum_{i=1}^N w(r_i) [G_{\text{obs}}(r_i) - G_{\text{calc}}(r_i)]^2}{\sum_{i=1}^N w(r_i) G_{\text{obs}}^2(r_i)}}$$

with  $G_{\text{obs}}$  and  $G_{\text{calc}}$  being the observed and calculated PDF and  $w(r_i)$  the weight for each data point.

**Raman Spectroscopy.** The samples used for Raman spectroscopy were prepared identically to the X-ray diffraction samples, that is, flame-sealed in Ar-filled 1 mm-diameter quartz capillaries. Spectra were measured using a Renishaw inVia Qontor confocal microscope equipped with a 532 nm laser excitation source. The sealed capillary was placed on a temperature-controlled stage (HFS600E-PB4, Linkam) for variable temperature experiments. Cooling was achieved using water or nitrogen flow for temperatures above and below ambient temperature, respectively. Spectra were collected in back-scattering geometry using a Centrus detector in the range  $-750$  to  $750 \text{ cm}^{-1}$  centered around the elastic peak (Stokes and anti-Stokes). Typically, spectra were continuously measured at a rate of 1 spectrum/minute while heating/cooling at  $5 \text{ }^\circ\text{C}/\text{min}$ . The incident power of the laser was set to 5 mW focused by a 10 $\times$  objective to a spot of around 10  $\mu\text{m}$  on the sample. These parameters were optimized to maximize the signal-over-noise ratio while avoiding excessive local heating and decomposition/melting of the sample.

**Inelastic Neutron Scattering.** Samples ( $\sim 2 \text{ g}$ ) for INS measurements were lightly compacted into pellets and sealed in 10 mm diameter  $\text{SiO}_2$  ampules under vacuum ( $\sim 10^{-2} \text{ mbar}$ ). The ampules were placed in custom-made Nb holders and subsequently in an evacuated furnace environment. Spectra were measured using the cold-neutron, time-of-flight, time-focusing, IN6 spectrometer at the Institut Laue-Langevin (ILL) in Grenoble, France. An incident wavelength of 5.12  $\text{\AA}$  was used, offering an elastic energy resolution of  $\sim 0.1 \text{ meV}$ , as determined from a standard vanadium sample. The vanadium sample was also used to calibrate the detectors. The measurements were carried out in the high-resolution, inelastic time focusing mode. The phonon spectra were collected in the up-scattering, neutron energy-gain mode up to 80 meV in terms of the GDOS. Data reduction and treatment, including detector efficiency calibration and background subtraction, were performed using standard ILL procedures implemented in the large array manipulation program (LAMP) package.<sup>85</sup> Data reduction included measuring an identical empty  $\text{SiO}_2$  ampule and Nb container under the same experimental conditions. The  $Q$ -averaged, multiphonon-corrected<sup>84</sup> GDOS,  $g^{(n)}(E)$ , was obtained within the incoherent approximation framework.<sup>85</sup>

**Thermal Analysis.** For determination of the heat capacity ( $c_p$ ), three DSC measurements were performed using a Netzsch DSC 204 F1 calorimeter in the range 30–600  $^\circ\text{C}$  at a heating rate of 10  $^\circ\text{C}/\text{min}$ . The blank signal was measured using two empty crucibles. A sapphire reference sample was measured using the same parameters, followed by the  $\text{Na}_3\text{PS}_4$  sample. The samples were placed in aluminum pans with pierced lids. The specific heat capacity (in  $\text{J g}^{-1} \text{ K}^{-1}$ ) was determined according to the ASTM E1269 protocol according to

$$c_p^{\text{sample}} = \frac{\text{DSC}^{\text{sample}} - \text{DSC}^{\text{blank}}}{m^{\text{sample}} \cdot \text{HR} \cdot \text{sensitivity}}$$

where DSC is the measured signal (in  $\mu\text{V}$ ),  $m$  is the sample mass (mg), HR the heating rate ( $\text{K}/\text{s}$ ), and sensitivity ( $\mu\text{V}/\text{mW}$ ) is defined by the reference measurement and the known heat capacity of sapphire

$$\text{sensitivity} = \frac{\text{DSC}^{\text{sapphire}} - \text{DSC}^{\text{blank}}}{m^{\text{sapphire}} \cdot \text{HR} \cdot c_p^{\text{sapphire}}}$$

For measurements up to 800  $^\circ\text{C}$ , thermogravimetric analysis and DSC measurements were performed simultaneously using a Netzsch Simultaneous thermal analyzer STA449F3 housed in an Ar-filled glovebox (Jacomex). Samples were placed on quartz holders to avoid reactions at temperatures  $>600 \text{ }^\circ\text{C}$ . The measurements were performed under flow of argon gas (60 mL/min) at a heating/cooling rate of 5  $^\circ\text{C}/\text{min}$ . Oxygen impurities in the argon gas were captured at temperatures of  $>300 \text{ }^\circ\text{C}$  by a metallic zirconium ring placed in-line before the sample.

**AIMD Simulation.** Calculations in this work were carried out using DFT with the Vienna Ab Initio Simulation Package (VASP).<sup>86</sup> A plane-wave cutoff energy of 400 eV was utilized for the AIMD calculations. The projector augmented wave method<sup>87</sup> and the PBEsol exchange–correlation functional<sup>88</sup> were employed. The  $k$ -space was sampled at the  $\Gamma$ -point only with a  $3 \times 3 \times 3$  supercell of the  $\alpha$ - $\text{Na}_3\text{PS}_4$  structure containing 432 atoms, and a  $3 \times 2 \times 1$  supercell of the  $\gamma$ - $\text{Na}_3\text{PS}_4$  structure<sup>46</sup> containing 384 atoms. No Na vacancies were added to the supercells. The AIMD simulations were carried out at 300 and 500 K in the  $\alpha$  phase and at 900 K in the  $\gamma$ -phase, with a time step of 2 fs. Statistical properties were obtained from  $>100 \text{ ps}$  simulations at 300 K,  $>72 \text{ ps}$  at 500 K, and  $>62 \text{ ps}$  at 900 K, using the NVT ensemble with a Nose–Hoover thermostat.<sup>89</sup>

**RDF Calculations.** Pair RDFs were extracted from the present AIMD simulations on  $\alpha$ - $\text{Na}_3\text{PS}_4$  and previously reported simulations on  $\gamma$ - $\text{Na}_3\text{PS}_4$ <sup>46</sup> in order to compare with the experimentally measured PDFs. The calculation of the RDFs was performed using the  $g(r)$  GUI, as implemented in the visual molecular dynamics suite.<sup>90</sup>

**GDOS Spectrum Calculations.** The partial atomistic vibrational densities of states were extracted from the AIMD simulations on  $\alpha$ - $\text{Na}_3\text{PS}_4$  (300 and 500 K) and  $\gamma$ - $\text{Na}_3\text{PS}_4$  (900 K) by performing a Fourier transform of the velocity autocorrelation function<sup>91</sup> of the trajectories of the different atom types (Na, P, and S). In order to compare directly with our INS-derived GDOS spectra, the calculated partial vibrational contributions of the different atoms were neutron-weighted to get the total calculated GDOS,  $g^{(n)}(E)$ . In contrast to the vibrational density of states, the GDOS involves a weighting of the scatterers (ions) with their scattering powers  $\sigma/M$  ( $\sigma$ : neutron scattering cross section,  $M$ : mass). The values of 0.143, 0.107, and 0.032  $\text{b}\cdot\text{amu}^{-1}$  were used for Na, P, and S, respectively.

The phonon band center average vibrational energy  $E_{\text{av}}$  was determined numerically, weighted by the (total or partial) GDOS as follows:

$$E_{\text{av}} = \frac{\int_{E=0}^{E_{\text{max}}} E \cdot g^{(n)}(E) \text{ d}E}{\int_{E=0}^{E_{\text{max}}} g^{(n)}(E) \text{ d}E}$$

Such  $E_{\text{av}}$  can be calculated for the total GDOS or the atom-projected partial GDOS, for example, for Na. To compare the sodium  $E_{\text{av}}$  from calculations to the experimental spectra, we calculated the  $E_{\text{av}}$  from the experimental spectra with an  $E_{\text{max}}$  of 30 meV under the reasonable assumption that the  $\text{Na}_3\text{PS}_4$  GDOS under this energy value are dominated by sodium.

**Vibrational Spectrum Calculations.** The vibrational spectra of  $\text{Na}_3\text{PS}_4$  were simulated using DFT as implemented in the all-electron code CRYSTAL17<sup>92,93</sup> where the crystalline wave functions are expanded as a linear combination of atomic orbitals and further expanded by a consistent triple- $\zeta$  and polarization basis-set.<sup>94,95</sup> The DFT total energy during the geometry relaxation and in the phonon calculations was converged within  $\sim 10^{-10}$  a.u. and integrated over a well converged and symmetrized  $8 \times 8 \times 8$   $k$ -point mesh. Forces and stresses were converged using the default convergence criteria. Whenever possible, the internal symmetry was maintained. The unknown exchange–correlation contribution to the total energy was approximated by a hybrid functional that combines the PBE-generalized gradient functional by Perdew, Burke, and Ernzerhof<sup>96</sup> with a predefined amount of exact exchange (25%), as proposed by

Adamo and Barone.<sup>97,98</sup> The truncation of the (infinite) Coulomb and exchange series was set by the tolerances (TOLINTEG):  $10^{-7}$ ,  $10^{-7}$ ,  $10^{-7}$ ,  $10^{-9}$ , and  $10^{-30}$  Hartree, while an XXLGRID was used for the integration of the charge density. Raman frequencies of the two polymorphs were computed at the  $\Gamma$ -point, employing the finite difference method. Thus, the dynamical matrix was developed using a step size of 0.003 Å for each displacement. The Raman intensities were computed via the coupled-perturbed Kohn–Sham method.<sup>99,100</sup>

## ■ ASSOCIATED CONTENT

### SI Supporting Information

The Supporting Information is available free of charge at <https://pubs.acs.org/doi/10.1021/acs.chemmater.1c01113>.

Combined Rietveld refinements of neutron and X-ray Bragg diffraction data sets at 30 and 300 °C, Le Bail refinements of neutron and X-ray Bragg diffractograms at 550 and 600 °C, respectively, small-box PDF refinements of neutron total-scattering data sets at 30 and 300 °C, visual comparison of neutron- and X-ray PDFs at 600 °C, group theoretical analysis of vibrational modes of  $\alpha$ - and  $\beta$ - $\text{Na}_3\text{PS}_4$ , total and Na-projected phonon band centers as a function of temperature, additional DSC experiments up to 800 °C and photographs of visual melting point determination, sequential X-ray Bragg diffractograms highlighting the  $\alpha$ -to- $\beta$  phase transition on heating and associated fitted parameters, evolution of the P–S bond length upon heating, theoretical background on the splitting of internal vibrational modes in molecular crystals and summary of experiments (PDF)

Crystallographic data for  $\alpha$ - $\text{Na}_3\text{PS}_4$  from combined refinement of neutron- and X-ray Bragg diffractograms measured at the 30 °C (CIF)

Crystallographic data for  $\alpha$ - $\text{Na}_3\text{PS}_4$  from refinement of the neutron PDF measured at 30 °C (CIF)

Crystallographic data for  $\beta$ - $\text{Na}_3\text{PS}_4$  from combined refinement of neutron- and X-ray Bragg diffractograms measured at 300 °C (CIF)

Crystallographic data for  $\beta$ - $\text{Na}_3\text{PS}_4$  from refinement of the neutron PDF measured at 300 °C (CIF)

Crystallographic data for  $\gamma$ - $\text{Na}_3\text{PS}_4$  from refinement of the X-ray Bragg diffractogram measured at 550 °C (CIF)

## ■ AUTHOR INFORMATION

### Corresponding Authors

**Theodosios Famprikis** – *Laboratoire de Réactivité et Chimie des Solides (LRCS), CNRS UMR 7314, Université de Picardie Jules Verne, 80039 Amiens, France; Department of Chemistry, University of Bath, BA2 7AY Bath, U.K.; ALISTORE European Research Institute, CNRS FR 3104, Amiens 80039, France; Réseau sur le Stockage Electrochimique de l'Énergie (RS2E), CNRS FR 3459, Amiens 80039, France; Present Address: Storage of Electrochemical Energy, Department of Radiation Science and Technology, Delft University of Technology, Delft, the Netherlands; [orcid.org/0000-0002-7946-1445](https://orcid.org/0000-0002-7946-1445); Email: [t.famprikis@tudelft.nl](mailto:t.famprikis@tudelft.nl)*

**M. Saiful Islam** – *Department of Chemistry, University of Bath, BA2 7AY Bath, U.K.; ALISTORE European Research Institute, CNRS FR 3104, Amiens 80039, France; [orcid.org/0000-0003-3882-0285](https://orcid.org/0000-0003-3882-0285); Email: [m.s.islam@bath.ac.uk](mailto:m.s.islam@bath.ac.uk)*

**Christian Masquelier** – *Laboratoire de Réactivité et Chimie des Solides (LRCS), CNRS UMR 7314, Université de Picardie Jules Verne, 80039 Amiens, France; ALISTORE European Research Institute, CNRS FR 3104, Amiens 80039, France; Réseau sur le Stockage Electrochimique de l'Énergie (RS2E), CNRS FR 3459, Amiens 80039, France; [orcid.org/0000-0001-7289-1015](https://orcid.org/0000-0001-7289-1015); Email: [christian.masquelier@u-picardie.fr](mailto:christian.masquelier@u-picardie.fr)*

### Authors

**Houssny Bouyanfif** – *Laboratoire de Physique de la Matière Condensée (LPMC), UR 2081, Université de Picardie Jules Verne, Amiens 80039, France*

**Pieremanuele Canepa** – *Department of Materials Science and Engineering, National University of Singapore, 117576, Singapore; Department of Chemical and Biomolecular Engineering, National University of Singapore, 117585, Singapore; [orcid.org/0000-0002-5168-9253](https://orcid.org/0000-0002-5168-9253)*

**Mohamed Zbiri** – *Institut Laue-Langevin (ILL), Grenoble 38042, France; [orcid.org/0000-0002-0413-0262](https://orcid.org/0000-0002-0413-0262)*

**James A. Dawson** – *Chemistry—School of Natural and Environmental Sciences and Centre for Energy, Newcastle University, Newcastle upon Tyne NE1 7RU, U.K.; [orcid.org/0000-0002-3946-5337](https://orcid.org/0000-0002-3946-5337)*

**Emmanuelle Suard** – *Institut Laue-Langevin (ILL), Grenoble 38042, France; [orcid.org/0000-0001-5966-5929](https://orcid.org/0000-0001-5966-5929)*

**François Fauth** – *CELLS—ALBA Synchrotron, ILL, Cerdanyola del Vallès 08290 Barcelona, Spain; [orcid.org/0000-0001-9465-3106](https://orcid.org/0000-0001-9465-3106)*

**Helen Y. Playford** – *ISIS Facility, Rutherford Appleton Laboratory, Didcot OX11 0QX, U.K.; [orcid.org/0000-0001-5445-8605](https://orcid.org/0000-0001-5445-8605)*

**Damien Dambournet** – *Physico-Chimie des Electrolytes et Nano-systèmes Interfaciaux (PHENIX), CNRS UMR 8234, Sorbonne Université, F-75005 Paris, France; Réseau sur le Stockage Electrochimique de l'Énergie (RS2E), CNRS FR 3459, Amiens 80039, France; [orcid.org/0000-0003-3831-2643](https://orcid.org/0000-0003-3831-2643)*

**Olaf J. Borkiewicz** – *X-ray Science Division, Advanced Photon Source, Argonne National Laboratory, Argonne, Illinois 60439, United States*

**Matthieu Courty** – *Laboratoire de Réactivité et Chimie des Solides (LRCS), CNRS UMR 7314, Université de Picardie Jules Verne, 80039 Amiens, France; Réseau sur le Stockage Electrochimique de l'Énergie (RS2E), CNRS FR 3459, Amiens 80039, France*

**Oliver Clemens** – *Materials Synthesis Group, Institute of Materials Science, University of Stuttgart, Stuttgart 70569, Germany; [orcid.org/0000-0002-0860-0911](https://orcid.org/0000-0002-0860-0911)*

**Jean-Noël Chotard** – *Laboratoire de Réactivité et Chimie des Solides (LRCS), CNRS UMR 7314, Université de Picardie Jules Verne, 80039 Amiens, France; Réseau sur le Stockage Electrochimique de l'Énergie (RS2E), CNRS FR 3459, Amiens 80039, France; [orcid.org/0000-0002-9867-7954](https://orcid.org/0000-0002-9867-7954)*

Complete contact information is available at: <https://pubs.acs.org/doi/10.1021/acs.chemmater.1c01113>

### Author Contributions

T.F. coordinated the work, synthesized the samples, and performed all experiments and analysis unless otherwise stated. H.B. assisted with Raman experiments and group theory analysis. P.C. performed the calculations of the vibrational spectra. M.Z. assisted with the neutron scattering experiments.

M.Z. and J.A.D. performed molecular dynamics simulations from which M.Z. extracted the neutron GDOS. E.S. and H.Y.P. assisted with the neutron diffraction experiments. H.Y.P. produced the neutron PDFs. F.F. performed the X-ray Bragg diffraction experiments. O.J.B. performed the X-ray total diffraction experiments and produced the PDFs. D.D. assisted with the analysis of the PDFs. M.C. performed the thermal analysis experiments. O.C., J.-N.C., M.S.I., and C.M. provided feedback and guidance. T.F. prepared the figures and wrote the manuscript with input from most authors.

## Notes

The authors declare no competing financial interest.

## ACKNOWLEDGMENTS

The authors are grateful to the Institut Laue-Langevin (ILL) for providing beam time on the D2B diffractometer for the powder diffraction measurements and the IN6 spectrometer for the INS measurements, to the ALBA synchrotron for providing beam time on the MSPD diffractometer for powder diffraction measurements, to the Argonne National Laboratory (ANL) for providing beam time on the 11-ID-B beamline of the Advanced Photon Source (APS) for the powder total scattering measurements, and to the ISIS neutron and muon source for providing beam time on the POLARIS diffractometer for powder total scattering measurements.<sup>101</sup> T.F. is thankful to the ALISTORE ERI and the German Academic Exchange Service (DAAD) for funding in the form of PhD scholarships. J.A.D. and M.S.I. gratefully acknowledge the EPSRC Programme Grant EP/M009521/1 for funding and the MCC/Archer consortium (EP/L000202/1) for computational resources. J.A.D. also gratefully acknowledges Newcastle University for funding through a Newcastle Academic Track (NUAcT) Fellowship. P.C. acknowledges funding from the National Research Foundation under his NRFF NRFF12-2020-0012 and the ANR-NRF NRF2019-NRF-ANR073 Na-MASTER. This research used resources of the Advanced Photon Source, a U.S. Department of Energy (DOE) Office of Science User Facility operated for the DOE Office of Science by the Argonne National Laboratory under contract no. DE-AC02-06CH11357.

## ADDITIONAL NOTES

<sup>a</sup>It remains an open question whether halide substitution (if indeed possible) would result in substitution of  $S^{2-}$  (i.e.,  $Na_{3-x}PS_{4-x}Cl_x$ ) or substitution of the entire polyanion (e.g.,  $Na_{3-2x}[PS_4]_{1-x}Cl_x$ ) in the  $Na_3PS_4$  structure.

<sup>b</sup>Computation of the Raman intensities with density functional theory is not a trivial task as these depend on the change of the polarizability tensor associated with the atomic displacements for each Raman mode. The calculation involves the assessment of the third derivative of the total energy with respect to the atomic displacements as the electric field is varied in two directions. Thus, the accuracy of such calculations is significantly affected by the lower-order derivatives of the total energies, which in turn depend on the approximation of density functional theory, including the choice of exchange and correlation functionals.

<sup>c</sup>A mode with a negative calculated frequency corresponds to a spontaneous displacement of atoms toward a lower energy configuration, in the present case, the tetragonal distortion of the cubic cell.

<sup>d</sup>There is also an argument for description of the  $\alpha$ -to- $\beta$  transition as an “order–disorder” one, given that the sodium positions in the  $\beta$ -polymorph are (slightly) better described by a 25%-occupied (i.e. disordered) 24f site. Nevertheless, the barycenter of sodium density remains on the 6b site, and we consider this aspect of the transition to be of secondary importance to the displacements of Na1 and S to higher symmetry positions, as illustrated in Figure 6.

<sup>e</sup>Note this nominal temperature is likely underestimated, see Figure S14.

## REFERENCES

- (1) Famprikis, T.; Canepa, P.; Dawson, J. A.; Islam, M. S.; Masquelier, C. Fundamentals of Inorganic Solid-State Electrolytes for Batteries. *Nat. Mater.* **2019**, *18*, 1278–1291.
- (2) Janek, J.; Zeier, W. G. A Solid Future for Battery Development. *Nat. Energy* **2016**, *1*, 16141.
- (3) Hasa, I.; Mariyappan, S.; Saurel, D.; Adelhelm, P.; Kuposov, A. Y.; Masquelier, C.; Croguennec, L.; Casas-Cabanas, M. Challenges of Today for Na-Based Batteries of the Future: From Materials to Cell Metrics. *J. Power Sources* **2021**, *482*, 228872.
- (4) Kudu, Ö. U.; Famprikis, T.; Fleutot, B.; Braidia, M.-D.; Le Mercier, T.; Islam, M. S.; Masquelier, C. A Review of Structural Properties and Synthesis Methods of Solid Electrolyte Materials in the  $Li_2S$ – $P_2S_5$  Binary System. *J. Power Sources* **2018**, *407*, 31–43.
- (5) Hayashi, A.; Noi, K.; Sakuda, A.; Tatsumisago, M. Superionic Glass-Ceramic Electrolytes for Room-Temperature Rechargeable Sodium Batteries. *Nat. Commun.* **2012**, *3*, 856.
- (6) Hayashi, A.; Noi, K.; Tanibata, N.; Nagao, M.; Tatsumisago, M. High Sodium Ion Conductivity of Glass–Ceramic Electrolytes with Cubic  $Na_3PS_4$ . *J. Power Sources* **2014**, *258*, 420–423.
- (7) Nguyen, H.; Banerjee, A.; Wang, X.; Tan, D.; Wu, E. A.; Doux, J.-M.; Stephens, R.; Verbist, G.; Meng, Y. S. Single-Step Synthesis of Highly Conductive  $Na_3PS_4$  Solid Electrolyte for Sodium All Solid-State Batteries. *J. Power Sources* **2019**, *435*, 126623.
- (8) Takeuchi, S.; Suzuki, K.; Hirayama, M.; Kanno, R. Sodium Superionic Conduction in Tetragonal  $Na_3PS_4$ . *J. Solid State Chem.* **2018**, *265*, 353–358.
- (9) Tanibata, N.; Deguchi, M.; Hayashi, A.; Tatsumisago, M. All-Solid-State Na/S Batteries with a  $Na_3PS_4$  Electrolyte Operating at Room Temperature. *Chem. Mater.* **2017**, *29*, 5232–5238.
- (10) Chu, I.-H.; Kompella, C. S.; Nguyen, H.; Zhu, Z.; Hy, S.; Deng, Z.; Meng, Y. S.; Ong, S. P. Room-Temperature All-Solid-State Rechargeable Sodium-Ion Batteries with a Cl-Doped  $Na_3PS_4$  Superionic Conductor. *Sci. Rep.* **2016**, *6*, 33733.
- (11) Yu, C.; Ganapathy, S.; de Klerk, N. J. J.; van Eck, E. R. H.; Wagemaker, M. Na-Ion Dynamics in Tetragonal and Cubic  $Na_3PS_4$ , a Na-Ion Conductor for Solid State Na-Ion Batteries. *J. Mater. Chem. A* **2016**, *4*, 15095–15105.
- (12) Tian, Y.; Shi, T.; Richards, W. D.; Li, J.; Kim, J. C.; Bo, S.-H.; Ceder, G. Compatibility Issues between Electrodes and Electrolytes in Solid-State Batteries. *Energy Environ. Sci.* **2017**, *10*, 1150–1166.
- (13) Yue, J.; Han, F.; Fan, X.; Zhu, X.; Ma, Z.; Yang, J.; Wang, C. High-Performance All-Inorganic Solid-State Sodium–Sulfur Battery. *ACS Nano* **2017**, *11*, 4885–4891.
- (14) Wan, H.; Mwizerwa, J. P.; Qi, X.; Xu, X.; Li, H.; Zhang, Q.; Cai, L.; Hu, Y. S.; Yao, X. Nanoscaled  $Na_3PS_4$  Solid Electrolyte for All-Solid-State  $FeS_2/Na$  Batteries with Ultrahigh Initial Coulombic Efficiency of 95% and Excellent Cyclic Performances. *ACS Appl. Mater. Interfaces* **2018**, *10*, 12300–12304.
- (15) Yue, J.; Zhu, X.; Han, F.; Fan, X.; Wang, L.; Yang, J.; Wang, C. Long Cycle Life All-Solid-State Sodium Ion Battery. *ACS Appl. Mater. Interfaces* **2018**, *10*, 39645–39650.
- (16) Pompe, C. Strukturchemie Und Elektrische Leitfähigkeiten von Natriumchalkogenometallaten. Dissertation, Universität Regensburg, 2016.

- (17) Bo, S.-H.; Wang, Y.; Ceder, G. Structural and Na-Ion Conduction Characteristics of  $\text{Na}_3\text{PS}_x\text{Se}_{4-x}$ . *J. Mater. Chem. A* **2016**, *4*, 9044–9053.
- (18) Kim, T. W.; Park, K. H.; Choi, Y. E.; Lee, J. Y.; Jung, Y. S. Aqueous-Solution Synthesis of  $\text{Na}_3\text{SbS}_4$  Solid Electrolytes for All-Solid-State Na-Ion Batteries. *J. Mater. Chem. A* **2018**, *6*, 840–844.
- (19) Wang, N.; Yang, K.; Zhang, L.; Yan, X.; Wang, L.; Xu, B. Improvement in Ion Transport in  $\text{Na}_3\text{PSe}_4$ – $\text{Na}_3\text{SbSe}_4$  by Sb Substitution. *J. Mater. Sci.* **2018**, *53*, 1987–1994.
- (20) Wang, H.; Chen, Y.; Hood, Z. D.; Keum, J. K.; Pandian, A. S.; Chi, M.; An, K.; Liang, C.; Sunkara, M. K. Revealing the Structural Stability and Na-Ion Mobility of 3D Superionic Conductor  $\text{Na}_3\text{SbS}_4$  at Extremely Low Temperatures. *ACS Appl. Energy Mater.* **2018**, *1*, 7028–7034.
- (21) Wang, H.; Yu, M.; Wang, Y.; Feng, Z.; Wang, Y.; Lü, X.; Zhu, J.; Ren, Y.; Liang, C. In-Situ Investigation of Pressure Effect on Structural Evolution and Conductivity of  $\text{Na}_3\text{SbS}_4$  Superionic Conductor. *J. Power Sources* **2018**, *401*, 111–116.
- (22) Wang, H.; Chen, Y.; Hood, Z. D.; Sahu, G.; Pandian, A. S.; Keum, J. K.; An, K.; Liang, C. An Air-Stable  $\text{Na}_3\text{SbS}_4$  Superionic Conductor Prepared by a Rapid and Economic Synthetic Procedure. *Angew. Chem., Int. Ed.* **2016**, *55*, 8551–8555.
- (23) Krauskopf, T.; Pompe, C.; Kraft, M. A.; Zeier, W. G. Influence of Lattice Dynamics on  $\text{Na}^+$  Transport in the Solid Electrolyte  $\text{Na}_3\text{PS}_{4-x}\text{Se}_x$ . *Chem. Mater.* **2017**, *29*, 8859–8869.
- (24) Zhang, L.; Yang, K.; Mi, J.; Lu, L.; Zhao, L.; Wang, L.; Li, Y.; Zeng, H.  $\text{Na}_3\text{PSe}_4$ : A Novel Chalcogenide Solid Electrolyte with High Ionic Conductivity. *Adv. Energy Mater.* **2015**, *5*, 1501294.
- (25) Zhang, L.; Zhang, D.; Yang, K.; Yan, X.; Wang, L.; Mi, J.; Xu, B.; Li, Y. Vacancy-Contained Tetragonal  $\text{Na}_3\text{SbS}_4$  Superionic Conductor. *Adv. Sci.* **2016**, *3*, 1600089.
- (26) Banerjee, A.; Park, K. H.; Heo, J. W.; Nam, Y. J.; Moon, C. K.; Oh, S. M.; Hong, S.-T.; Jung, Y. S.  $\text{Na}_3\text{SbS}_4$ : A Solution Processable Sodium Superionic Conductor for All-Solid-State Sodium-Ion Batteries. *Angew. Chem., Int. Ed.* **2016**, *55*, 9634–9638.
- (27) Yu, Z.; Shang, S. L.; Seo, J. H.; Wang, D.; Luo, X.; Huang, Q.; Chen, S.; Lu, J.; Li, X.; Liu, Z. K.; et al. Exceptionally High Ionic Conductivity in  $\text{Na}_3\text{P}_{0.62}\text{As}_{0.38}\text{S}_4$  with Improved Moisture Stability for Solid-State Sodium-Ion Batteries. *Adv. Mater.* **2017**, *29*, 1605561.
- (28) Shang, S.-L.; Yu, Z.; Wang, Y.; Wang, D.; Liu, Z.-K. Origin of Outstanding Phase and Moisture Stability in a  $\text{Na}_3\text{P}_{1-x}\text{As}_x\text{S}_4$  Superionic Conductor. *ACS Appl. Mater. Interfaces* **2017**, *9*, 16261–16269.
- (29) Rush, L. E.; Hood, Z. D.; Holzwarth, N. A. W. Unraveling the Electrolyte Properties of  $\text{Na}_3\text{SbS}_4$  through Computation and Experiment. *Phys. Rev. Mater.* **2017**, *1*, 075405.
- (30) Xiong, S.; Liu, Z.; Rong, H.; Wang, H.; McDaniel, M.; Chen, H.  $\text{Na}_3\text{SbSe}_{4-x}\text{S}_x$  as Sodium Superionic Conductors. *Sci. Rep.* **2018**, *8*, 9146.
- (31) Moon, C. K.; Lee, H.-J.; Park, K. H.; Kwak, H.; Heo, J. W.; Choi, K.; Yang, H.; Kim, M.-S.; Hong, S.-T.; Lee, J. H.; et al. Vacancy-Driven  $\text{Na}^+$  Superionic Conduction in New Ca-Doped  $\text{Na}_3\text{PS}_4$  for All-Solid-State Na-Ion Batteries. *ACS Energy Lett.* **2018**, *3*, 2504–2512.
- (32) De Klerk, N. J. J.; Wagemaker, M. Diffusion Mechanism of the Sodium-Ion Solid Electrolyte  $\text{Na}_3\text{PS}_4$  and Potential Improvements of Halogen Doping. *Chem. Mater.* **2016**, *28*, 3122–3130.
- (33) Wu, E. A.; Kompella, C. S.; Zhu, Z.; Lee, J. Z.; Lee, S. C.; Chu, I.-H.; Nguyen, H.; Ong, S. P.; Banerjee, A.; Meng, Y. S. New Insights into the Interphase between the Na Metal Anode and Sulfide Solid-State Electrolytes: A Joint Experimental and Computational Study. *ACS Appl. Mater. Interfaces* **2018**, *10*, 10076–10086.
- (34) Feng, X.; Chien, P. H.; Zhu, Z.; Chu, I. H.; Wang, P.; Immediato-Scuotto, M.; Arabzadeh, H.; Ong, S. P.; Hu, Y. Y. Studies of Functional Defects for Fast Na-Ion Conduction in  $\text{Na}_{3-y}\text{PS}_{4-x}\text{Cl}_x$  with a Combined Experimental and Computational Approach. *Adv. Funct. Mater.* **2019**, *29*, 1807951.
- (35) Uematsu, M.; Yubuchi, S.; Tsuji, F.; Sakuda, A.; Hayashi, A.; Tatsumisago, M. Suspension Synthesis of  $\text{Na}_{3-x}\text{PS}_{4-x}\text{Cl}_x$  Solid Electrolytes. *J. Power Sources* **2019**, *428*, 131–135.
- (36) Tanibata, N.; Noi, K.; Hayashi, A.; Kitamura, N.; Idemoto, Y.; Tatsumisago, M. X-Ray Crystal Structure Analysis of Sodium-Ion Conductivity in  $94 \text{ Na}_3\text{PS}_4 \cdot 6 \text{ Na}_4\text{SiS}_4$  Glass-Ceramic Electrolytes. *ChemElectroChem* **2014**, *1*, 1130–1132.
- (37) Tanibata, N.; Noi, K.; Hayashi, A.; Tatsumisago, M. Preparation and Characterization of Highly Sodium Ion Conducting  $\text{Na}_3\text{PS}_4$ – $\text{Na}_4\text{SiS}_4$  Solid Electrolytes. *RSC Adv.* **2014**, *4*, 17120–17123.
- (38) Zhu, Z.; Chu, I.-H.; Deng, Z.; Ong, S. P. Role of  $\text{Na}^+$  Interstitials and Dopants in Enhancing the  $\text{Na}^+$  Conductivity of the Cubic  $\text{Na}_3\text{PS}_4$  Superionic Conductor. *Chem. Mater.* **2015**, *27*, 8318–8325.
- (39) Fuchs, T.; Culver, S. P.; Till, P.; Zeier, W. G. Defect-Mediated Conductivity Enhancements in  $\text{Na}_{3-x}\text{Pn}_{1-x}\text{W}_x\text{S}_4$  (Pn = P, Sb) Using Alivalent Substitutions. *ACS Energy Lett.* **2020**, *5*, 146–151.
- (40) Hayashi, A.; Masuzawa, N.; Yubuchi, S.; Tsuji, F.; Hotehama, C.; Sakuda, A.; Tatsumisago, M. A Sodium-Ion Sulfide Solid Electrolyte with Unprecedented Conductivity at Room Temperature. *Nat. Commun.* **2019**, *10*, 5266.
- (41) Gamo, H.; Nguyen, H. H. P.; Matsuda, R.; Muto, H.; Matsuda, A.  $\text{Na}_{3+x}(\text{Sb}_{1-x}\text{Sn}_x)\text{S}_4$  Solid Electrolytes ( $0 \leq x \leq 0.1$ ) as Sodium Ion Conductors. *Solid State Ionics* **2020**, *344*, 115133.
- (42) Jalem, R.; Hayashi, A.; Tsuji, F.; Sakuda, A.; Tateyama, Y. First-Principles Calculation Study of  $\text{Na}^+$  Superionic Conduction Mechanism in W- and Mo-Doped  $\text{Na}_3\text{SbS}_4$  Solid Electrolytes. *Chem. Mater.* **2020**, *32*, 8373–8381.
- (43) Tsuji, F.; Masuzawa, N.; Sakuda, A.; Tatsumisago, M.; Hayashi, A. Preparation and Characterization of Cation-Substituted  $\text{Na}_3\text{SbS}_4$  Solid Electrolytes. *ACS Appl. Energy Mater.* **2020**, *3*, 11706–11712.
- (44) Yubuchi, S.; Ito, A.; Masuzawa, N.; Sakuda, A.; Hayashi, A.; Tatsumisago, M. Aqueous Solution Synthesis of  $\text{Na}_3\text{SbS}_4$ – $\text{Na}_2\text{WS}_4$  Superionic Conductors. *J. Mater. Chem. A* **2020**, *8*, 1947–1954.
- (45) Famprikis, T.; Kudu, Ö. U.; Dawson, J. A.; Canepa, P.; Fauth, F.; Suard, E.; Zbiri, M.; Dambournet, D.; Borkiewicz, O. J.; Bouyanfif, H.; et al. Under Pressure: Mechanochemical Effects on Structure and Ion Conduction in the Sodium-Ion Solid Electrolyte  $\text{Na}_3\text{PS}_4$ . *J. Am. Chem. Soc.* **2020**, *142*, 18422–18436.
- (46) Famprikis, T.; Dawson, J. A.; Fauth, F.; Clemens, O.; Suard, E.; Fleutot, B.; Courty, M.; Chotard, J.-N.; Islam, M. S.; Masquelier, C. A New Superionic Plastic Polymorph of the  $\text{Na}^+$  Conductor  $\text{Na}_3\text{PS}_4$ . *ACS Mater. Lett.* **2019**, *1*, 641–646.
- (47) Jansen, M.; Henseler, U. Synthesis, Structure Determination, and Ionic Conductivity of Sodium Tetrathiosulfate. *J. Solid State Chem.* **1992**, *99*, 110–119.
- (48) Nishimura, S.-i.; Tanibata, N.; Hayashi, A.; Tatsumisago, M.; Yamada, A. The Crystal Structure and Sodium Disorder of High-Temperature Polymorph  $\beta$ - $\text{Na}_3\text{PS}_4$ . *J. Mater. Chem. A* **2017**, *5*, 25025–25030.
- (49) Poulet, H.; Mathieu, J. P. *Vibration Spectra and Symmetry of Crystals*; Gordon & Breach: New York, 1976.
- (50) Rousseau, D. L.; Bauman, R. P.; Porto, S. P. S. Normal Mode Determination in Crystals. *J. Raman Spectrosc.* **1981**, *10*, 253–290.
- (51) Krauskopf, T.; Muy, S.; Culver, S. P.; Ohno, S.; Delaire, O.; Shao-Horn, Y.; Zeier, W. G. Comparing the Descriptors for Investigating the Influence of Lattice Dynamics on Ionic Transport Using the Superionic Conductor  $\text{Na}_3\text{PS}_{4-x}\text{Se}_x$ . *J. Am. Chem. Soc.* **2018**, *140*, 14464–14473.
- (52) Blachnik, R.; Rabe, U. Das Thermische Verhalten Der Mischungen  $\text{Na}_2\text{S-P}_4\text{S}_{10}$  Und  $\text{Na}_4\text{Ge}_4\text{S}_{10-P}_4\text{S}_{10}$  Des Systems  $\text{Na}_2\text{S-GeS}_2\text{-P}_4\text{S}_{10}$ . *Z. Anorg. Allg. Chem.* **1980**, *462*, 199–206.
- (53) Jaeger, G. The Ehrenfest Classification of Phase Transitions: Introduction and Evolution. *Arch. Hist. Exact Sci.* **1998**, *53*, 51–81.
- (54) Seidel, S.; Zeier, W. G.; Pöttgen, R. The Polymorphs of the  $\text{Na}^+$  Ion Conductor  $\text{Na}_3\text{PS}_4$  Viewed from the Perspective of a Group-Subgroup Scheme. *Z. Kristallogr.—Cryst. Mater.* **2020**, *235*, 1–6.
- (55) Krauskopf, T.; Culver, S. P.; Zeier, W. G. Local Tetragonal Structure of the Cubic Superionic Conductor  $\text{Na}_3\text{PS}_4$ . *Inorg. Chem.* **2018**, *57*, 4739–4744.

- (56) Krauskopf, T.; Culver, S. P.; Zeier, W. G. Bottleneck of Diffusion and Inductive Effects in  $\text{Li}_{10}\text{Ge}_{1-x}\text{Sn}_x\text{P}_2\text{S}_{12}$ . *Chem. Mater.* **2018**, *30*, 1791–1798.
- (57) Culver, S. P.; Squires, A. G.; Minafra, N.; Armstrong, C. W. F.; Krauskopf, T.; Böcher, F.; Li, C.; Morgan, B. J.; Zeier, W. G. Evidence for a Solid-Electrolyte Inductive Effect in the Superionic Conductor  $\text{Li}_{10}\text{Ge}_{1-x}\text{Sn}_x\text{P}_2\text{S}_{12}$ . *J. Am. Chem. Soc.* **2020**, *142*, 21210–21219.
- (58) Sau, K.; Ikeshoji, T. Origin of Fast Ion Conduction in  $\text{Na}_3\text{PS}_4$ : Insight from Molecular Dynamics Study. *J. Phys. Chem. C* **2020**, *124*, 20671–20681.
- (59) Funnell, N. P.; Dove, M. T.; Goodwin, A. L.; Parsons, S.; Tucker, M. G. Local Structure Correlations in Plastic Cyclohexane—a Reverse Monte Carlo Study. *J. Phys. Condens. Matter* **2013**, *25*, 454204.
- (60) Dawson, J. A.; Canepa, P.; Clarke, M. J.; Famprikis, T.; Ghosh, D.; Islam, M. S. Toward Understanding the Different Influences of Grain Boundaries on Ion Transport in Sulfide and Oxide Solid Electrolytes. *Chem. Mater.* **2019**, *31*, 5296–5304.
- (61) Nilsson, L.; Thomas, J. O.; Tofield, B. C. The Structure of the High-Temperature Solid Electrolyte Lithium Sulphate at 908K. *J. Phys. C: Solid State Phys.* **1980**, *13*, 6441–6451.
- (62) Wiench, D. M.; Jansen, M. Über  $\text{Na}_3\text{PO}_4$ : Versuche Zur Reindarstellung, Kristallstruktur Der Hochtemperaturform. *Z. Anorg. Allg. Chem.* **1980**, *461*, 101–108.
- (63) Harrison, R. J.; Putnis, A.; Kockelmann, W. Phase Transition Behaviour and Equilibrium Phase Relations in the Fast-Ion Conductor System  $\text{Na}_3\text{PO}_4$ – $\text{Na}_2\text{SO}_4$ . *Phys. Chem. Chem. Phys.* **2002**, *4*, 3252–3259.
- (64) Saha, S.; Rousse, G.; Courty, M.; Shakhova, Y.; Kirsanova, M.; Fauth, F.; Pomjakushin, V.; Abakumov, A. M.; Tarascon, J. M. Structural Polymorphism in  $\text{Na}_4\text{Zn}(\text{PO}_4)_2$  Driven by Rotational Order–Disorder Transitions and the Impact of Heterovalent Substitutions on Na-Ion Conductivity. *Inorg. Chem.* **2020**, *59*, 6528–6540.
- (65) Soldate, A. M. Crystal Structure of Sodium Borohydride. *J. Am. Chem. Soc.* **1947**, *69*, 987–988.
- (66) Abrahams, S. C.; Kalnajs, J. The Lattice Constants of the Alkali Borohydrides and the Low-Temperature Phase of Sodium Borohydride. *J. Chem. Phys.* **1954**, *22*, 434–436.
- (67) Kim, M. I.; Wakada, T.; Akasaka, S.; Nishitsuji, S.; Saijo, K.; Hasegawa, H.; Ito, K.; Takenaka, M. Stability of the *Fddd* Phase in Diblock Copolymer Melts. *Macromolecules* **2008**, *41*, 7667–7670.
- (68) Miao, B.; Wickham, R. A. Fluctuation Effects and the Stability of the *Fddd* Network Phase in Diblock Copolymer Melts. *J. Chem. Phys.* **2008**, *128*, 054902.
- (69) Kim, M. I.; Wakada, T.; Akasaka, S.; Nishitsuji, S.; Saijo, K.; Hasegawa, H.; Ito, K.; Takenaka, M. Determination of the *Fddd* Phase Boundary in Polystyrene-Block-Polyisoprene Diblock Copolymer Melts. *Macromolecules* **2009**, *42*, 5266–5271.
- (70) Yamada, K.; Nonomura, M.; Ohta, T. *Fddd* Structure in AB-Type Diblock Copolymers. *J. Phys. Condens. Matter* **2006**, *18*, L421.
- (71) Takenaka, M.; Wakada, T.; Akasaka, S.; Nishitsuji, S.; Saijo, K.; Shimizu, H.; Kim, M. I.; Hasegawa, H. Orthorhombic *Fddd* Network in Diblock Copolymer Melts. *Macromolecules* **2007**, *40*, 4399–4402.
- (72) Tyler, C. A.; Morse, D. C. Orthorhombic *Fddd* Network in Triblock and Diblock Copolymer Melts. *Phys. Rev. Lett.* **2005**, *94*, 208302.
- (73) Bailey, T. S.; Hardy, C. M.; Epps, T. H.; Bates, F. S. A Noncubic Triply Periodic Network Morphology in Poly(Isoprene-*b*-Styrene-*b*-Ethylene Oxide) Triblock Copolymers. *Macromolecules* **2002**, *35*, 7007–7017.
- (74) Epps, T. H.; Cochran, E. W.; Hardy, C. M.; Bailey, T. S.; Waletzko, R. S.; Bates, F. S. Network Phases in ABC Triblock Copolymers. *Macromolecules* **2004**, *37*, 7085–7088.
- (75) Agosta, L.; Metere, A.; Oleynikov, P.; Dzugutov, M. Self-Assembly of a Triply Periodic Continuous Mesophase with *Fddd* Symmetry in Simple One-Component Liquids. *J. Chem. Phys.* **2020**, *152*, 191101.
- (76) Fauth, F.; Peral, I.; Popescu, C.; Knapp, M. The New Material Science Powder Diffraction Beamline at ALBA Synchrotron. *Powder Diffr.* **2013**, *28*, S360–S370.
- (77) Fauth, F.; Boer, R.; Gil-Ortiz, F.; Popescu, C.; Vallcorba, O.; Peral, I.; Fullà, D.; Benach, J.; Juanhuix, J. The Crystallography Stations at the Alba Synchrotron. *Eur. Phys. J. Plus* **2015**, *130*, 160.
- (78) Rodríguez-Carvajal, J.; Roisnel, T. Line Broadening Analysis Using FullProf®: Determination of Microstructural Properties. *Mater. Sci. Forum* **2004**, *443–444*, 123–126.
- (79) Petříček, V.; Dušek, M.; Palatinus, L. Crystallographic Computing System JANA2006: General Features. *Z. Kristallogr.* **2014**, *229*, 345–352.
- (80) Thompson, P.; Cox, D. E.; Hastings, J. B. Rietveld Refinement of Debye–Scherrer Synchrotron X-Ray Data from  $\text{Al}_2\text{O}_3$ . *J. Appl. Crystallogr.* **1987**, *20*, 79–83.
- (81) Farrow, C. L.; Juhas, P.; Liu, J. W.; Bryndin, D.; Božin, E. S.; Bloch, J.; Proffen, T.; Billinge, S. J. L. PDFfit2 and PDFgui: Computer Programs for Studying Nanostructure in Crystals. *J. Phys. Condens. Matter* **2007**, *19*, 335219.
- (82) Soper, A. K. GudrunN and GudrunX Programs: Programs for Correcting Raw Neutron and x-Ray Diffraction Data to Differential Scattering Cross Section. *Rutherford Applet. Lab. Tech. Reports* **2011**, RAL-TR-201.
- (83) Richard, D.; Ferrand, M.; Kearley, G. J. Analysis and Visualisation of Neutron-Scattering Data. *J. Neutron Res.* **1996**, *4*, 33–39.
- (84) Sjölander, A. Multi-Phonon Processes in Slow Neutron Scattering by Crystals. *Ark. Fys.* **1958**, *14*, 315.
- (85) Skold, K.; Price, D. *Neutron Scattering*; Academic Press; Vol. 23A, 1986.
- (86) Kresse, G.; Furthmüller, J. Efficient Iterative Schemes for Ab Initio Total-Energy Calculations Using a Plane-Wave Basis Set. *Phys. Rev. B: Condens. Matter Mater. Phys.* **1996**, *54*, 11169–11186.
- (87) Blöchl, P. E. Projector Augmented-Wave Method. *Phys. Rev. B: Condens. Matter Mater. Phys.* **1994**, *50*, 17953–17979.
- (88) Perdew, J. P.; Ruzsinszky, A.; Csonka, G. I.; Vydrov, O. A.; Scuseria, G. E.; Constantin, L. A.; Zhou, X.; Burke, K. Restoring the Density-Gradient Expansion for Exchange in Solids and Surfaces. *Phys. Rev. Lett.* **2008**, *100*, 136406.
- (89) Evans, D. J.; Holian, B. L. The Nose–Hoover Thermostat. *J. Chem. Phys.* **1985**, *83*, 4069–4074.
- (90) Humphrey, W.; Dalke, A.; Schulten, K. VMD: Visual Molecular Dynamics. *J. Mol. Graph.* **1996**, *14*, 33–38.
- (91) Dickey, J. M.; Paskin, A. Computer Simulation of the Lattice Dynamics of Solids. *Phys. Rev.* **1969**, *188*, 1407–1418.
- (92) Dovesi, R.; Erba, A.; Orlando, R.; Zicovich-Wilson, C. M.; Civalieri, B.; Maschio, L.; Rérat, M.; Casassa, S.; Baima, J.; Salustro, S.; et al. Quantum-Mechanical Condensed Matter Simulations with CRYSTAL. *Wiley Interdiscip. Rev.: Comput. Mol. Sci.* **2018**, *8*, No. e1360.
- (93) Dovesi, R.; Saunders, V. R.; Roetti, C.; Orlando, R.; Zicovich-Wilson, C. M.; Pascale, F.; Civalieri, B.; Doll, K.; Harrison, N. M.; Bush, I. J.; et al. *CRYSTAL17. User's Manual*; University of Torino: Torino, 2018.
- (94) Laun, J.; Vilela Oliveira, D.; Bredow, T. Consistent Gaussian Basis Sets of Double- and Triple-Zeta Valence with Polarization Quality of the Fifth Period for Solid-State Calculations. *J. Comput. Chem.* **2018**, *39*, 1285–1290.
- (95) Peintinger, M. F.; Oliveira, D. V.; Bredow, T. Consistent Gaussian Basis Sets of Triple-Zeta Valence with Polarization Quality for Solid-State Calculations. *J. Comput. Chem.* **2013**, *34*, 451–459.
- (96) Perdew, J. P.; Burke, K.; Ernzerhof, M. Generalized Gradient Approximation Made Simple. *Phys. Rev. Lett.* **1996**, *77*, 3865–3868.
- (97) Perdew, J. P.; Ernzerhof, M.; Burke, K. Rationale for Mixing Exact Exchange with Density Functional Approximations. *J. Chem. Phys.* **1996**, *105*, 9982–9985.
- (98) Adamo, C.; Barone, V. Toward Reliable Density Functional Methods without Adjustable Parameters: The PBE0 Model. *J. Chem. Phys.* **1999**, *110*, 6158–6170.

(99) Ferrero, M.; Rérat, M.; Kirtman, B.; Dovesi, R. Calculation of First and Second Static Hyperpolarizabilities of One- to Three-Dimensional Periodic Compounds. Implementation in the CRYSTAL Code. *J. Chem. Phys.* **2008**, *129*, 244110.

(100) Maschio, L.; Kirtman, B.; Rérat, M.; Orlando, R.; Dovesi, R. Ab Initio Analytical Raman Intensities for Periodic Systems through a Coupled Perturbed Hartree-Fock/Kohn-Sham Method in an Atomic Orbital Basis. I. Theory. *J. Chem. Phys.* **2013**, *139*, 164101.

(101) Masquelier, C.; Morisset, A.; Smith, R.; Playford, H.; Famprikis, T. Elucidation of Dynamic Structural Characteristics of  $\gamma$ -Na<sub>3</sub>PS<sub>4</sub> Plastic Crystal through Neutron-PDF. *STFC ISIS Neutron and Muon Source*, 2019.